

UNIVERSITÉ LIBRE DE BRUXELLES

FACULTÉ DES SCIENCES

DÉPARTEMENT DE PHYSIQUE

SERVICE DE PHYSIQUE DES SYSTÈMES COMPLEXES ET MÉCANIQUE STATISTIQUE

Année académique 2019-2020

Phase diagrams from classical DFT computations

Auteur: Cédric SCHOONEN

Directeur: James F. LUTSKO

Co-Directeur: Pierre GASPARD



MÉMOIRE PRÉSENTÉ EN VUE DE L'OBTENTION DU DIPLÔME DE
MASTER EN SCIENCES PHYSIQUES.

Remerciements

Tout d'abord, je tiens à remercier James F. Lutsko et Pierre Gaspard pour la supervision de ce mémoire et leurs commentaires qui m'ont aidé à mener ce travail à bien. In particular, I would like to thanks James F. Lutsko who proposed me this subject and with whom I worked regularly.

Ensuite, j'aimerais remercier Caroline Jonas, Maxime Jamotte ainsi que ma mère pour la relecture critique, ou simplement orthographique, de ce travail. De plus, je remercie Maxime Jamotte pour nos nombreuses discussions tout au long de nos études. Nos échanges ont entretenu ma motivation, permis de réaliser mes erreurs et ont attiré mon attention sur de nombreux points que je n'aurais pas approfondis autrement.

Pour finir, je tiens à souligner le rôle déterminant de Mr. Claude De Bakker, mon professeur de Chimie, dans mon initiation scientifique durant mes années passées dans l'enseignement secondaire. Mr. De Bakker est un professeur exemplaire, qui a toujours pris le temps de répondre à mes nombreuses questions, bien souvent par des démonstrations directes.

Contents

1	Introduction	6
1.1	Motivations	6
1.2	Context: modern approaches to nucleation	7
1.3	Overview of this work	10
2	Density functional theory	13
2.1	Introduction	13
2.2	The grand canonical ensemble	13
2.3	The fundamental theorem of DFT	14
2.4	Properties of the density functional	16
2.5	Fundamental measure theory	18
2.6	Continuous potentials	20
3	DFT model: implementation and minimisation	23
3.1	The DFT model	23
3.2	Evaluation of the DFT functional	24
3.3	The case of a uniform density	25
3.4	Minimisation for fluid phases	26
3.5	Parametrisation of the solid density	29
3.6	Minimisation over gaussian profiles	31
3.7	Minimisation over lattice sizes	33
4	Coexistence curves	35
4.1	Generalities	35
4.2	The vapour-liquid coexistence	36
4.3	The fluid-solid coexistence	38
4.4	Extraction from simulation data	39
5	Phase diagrams	41
5.1	Introduction	41
5.2	Simple fluids	42
5.3	Colloids	44
6	Critical and triple points	46
6.1	Critical point	46
6.2	Triple point	51
7	Vacancy concentrations	52

7.1	Vacancies along coexistence curves	52
7.2	Comparison with simulations	54
8	FCC-HCP polymorphism	57
8.1	Implementation	57
8.2	Results	59
9	Conclusions and perspectives	63
A	Notations and units	65
A.1	Units	65
A.2	List of symbols	65
A.3	List of abbreviations	67
B	Computation details for chapter 2	68
B.1	Separation of the field-independent part of the free energy functional	68
B.2	Integration of the Euler-Lagrange equation: The density functional of the ideal gas	69
B.3	The uniform density limit of the mRSLT functional and the Carnahan- Starling equation of state	71
C	Free energy landscape for gaussian profiles	72
D	Code repository	75
	Bibliography	76

Abstract

In this project we apply tools from classical density functional theory (DFT) to compute phase diagrams for simple fluid and colloid potentials. We use a DFT model which treats the repulsive core as an effective hard sphere interaction and the attractive tail in a mean field way. The hard sphere part is modelled with fundamental measure theory (FMT) using a numerically stable functional. We also compute the concentration of vacancies in the solid and discuss the relative stability of the FCC and HCP lattice configurations. The motivation for this work is to study crystallisation in proteins using DFT to describe the energetics of the system. The objective is to determine whether the DFT model is able to reproduce the qualitative phase behaviour of proteins, as this is essential to describe the nucleation process.

Key words: Phase diagram, DFT, Nucleation, Proteins, Lattice vacancies

Résumé

Dans ce projet, nous utilisons les outils de la théorie de la fonctionnelle de densité (DFT) pour calculer des diagrammes de phases pour des potentiels de fluides simples et colloïdes. Nous utilisons un modèle DFT qui traite le noyau répulsif comme une interaction effective de sphères dures et la queue attractive à l'aide d'une théorie de champ moyen. La partie de sphères dures est modélisée avec la "théorie des mesures fondamentales" (FMT) en utilisant une fonctionnelle stable numériquement. Nous calculons également la concentration en trous dans le solide et discutons de la stabilité relative des configurations FCC et HCP. La motivation derrière ce travail est d'étudier la cristallisation des protéines en utilisant la DFT pour décrire les aspects énergétiques du processus. L'objectif est de vérifier que le modèle DFT est capable de reproduire les phases attendues pour un système de protéines, au moins d'un point de vue qualitatif. Cette propriété est en effet essentielle pour décrire le processus de nucléation.

Mots clés: Diagramme de phase, DFT, Nucléation, Protéines, Concentration de trous

Chapter 1

Introduction

1.1 Motivations

An important property of any material is its phase diagram. Understanding it is a crucial step in studying more complex phenomena such as nucleation, multiphase flow, etc. At the microscopic level, interactions between particles in the material are usually modelled using a potential whose parameters are chosen to best reproduce experimental data. However, which phases arise from this potential and where phase transitions lie are non trivial questions. Even simple, spherically symmetric potentials can exhibit qualitatively different phase diagrams. For example, Fig. 1.1 shows how the range of the attractive part of a simple potential can lead either to a "simple fluid" phase diagram, with vapour and liquid phases, or a phase diagram typical of macromolecules in solution (e.g. proteins) as well as colloids.

Several methods exist to compute the thermodynamic properties of a system, such as the phase diagram, beginning with a microscopic interaction potential. A common way is to use simulation techniques, such as molecular dynamics or Monte Carlo methods. They have the advantage of returning exact results, although subject to statistical uncertainties. In this work, we will instead use classical density functional theory (cDFT, or simply DFT). DFT provides state-of-the-art tools for studying the thermodynamics of both homogeneous and inhomogeneous systems, down to molecular length scales, using the interaction potential as single input. DFT models are however approximations of the real system and do not return exact results. The choice of using DFT comes from the context of this work, which is the study of nucleation.

Nucleation, and crystallisation in particular, attracts a lot of attention because of its widespread importance in many areas of science. Crystallisation plays a role in Alzheimer's disease [1] [2] and is an important process in the life of the malaria parasite, where its inhibition could be a way of treating the disease [3]. Crystallisation is also important for the production of pharmaceuticals, because drugs have to be

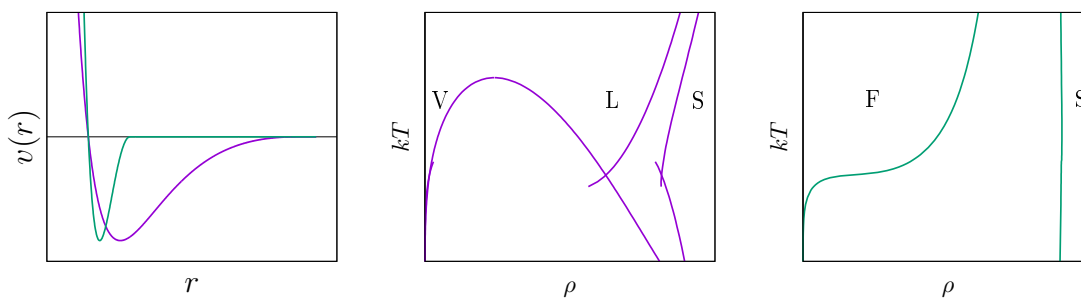


Figure 1.1 – Very different phase diagrams can be obtained simply by changing the range of the potential. The image on the left shows two spherically symmetric potentials with different attraction ranges. The other two images show the shape of the associated phase diagram. Labels V,L,S,F indicate vapour,liquid,solid and single fluid phases, respectively. See chapter 5 for more details.

produced in a particular polymorph. Control of the crystallisation process is thus a primary concern [4]. Until now, the naive picture of nucleation has been that a few molecules aggregate to form a small cluster of the new phase, which then grows or disappears as a result of random addition or removal of molecules. In recent years, this picture has been challenged by the discovery of non-classical effects in many systems of interest, most notably proteins [5, 6, 7, 8]. These effects show that the nucleation process is much more complex than previously thought.

The goal of this work is to establish whether the tools of DFT are sufficient to describe the different types of phase behaviour for a set of interaction potentials. It is a necessary first step to try to extend modern techniques to study crystallisation in proteins.

1.2 Context: modern approaches to nucleation

In this section, we provide a summary of the state of the art on the topic of nucleation. The objective is to set the context of this work and show the role of DFT in this subject.

In first order phase transitions, there is a free energy barrier between the initial and final states. The energy required to cross this barrier comes from thermal fluctuations and scales as the volume of the system undergoing the transformation. If the entire system were to transform at once, a huge energy would be required. So, the transformation happens in a restricted volume via the formation of small clusters of the new phase as a result of random fluctuations. Small clusters are unstable but if one happens to exceed a critical size, it becomes stable and then grows indefinitely. The fluctuation-driven first stage of the process is what is called nucleation.

The usual way of describing nucleation is with Classical Nucleation Theory (CNT) [9]. In CNT, the cluster is modelled as a macroscopic object of volume V , delimited by a sharp interface of area A . The excess free energy at the interface is taken into account by the surface tension γ . This representation of the cluster is called the capillary model. In this picture, the free energy difference between the cluster and the same region of the initial phase is given by

$$\Delta\Omega(A, V) = V\Delta\omega + A\gamma, \quad (1.1)$$

where $\Delta\omega$ is the free energy per unit volume difference between the final and initial phases. For small clusters, the surface term dominates so the excess free energy increases as the cluster size increases: such clusters are therefore thermodynamically driven to become smaller and to dissipate. For large enough clusters, the volume term dominates and the free energy then decreases with increasing cluster size so they are thermodynamically driven to grow. The transition between the two is called the critical cluster.

In the standard form of CNT, the dynamics of cluster growth consists of attachment and detachment of monomers to and from the cluster. For a spherically symmetric cluster, the attachment and detachment rates f_N and g_N only depend on the number of molecules in the cluster, N . The detachment rates can be expressed from the attachment rates with the assumption of detailed balance, which is delicate to justify as the system is actually out of equilibrium. Taking a continuous limit, we find a Fokker-Planck equation called the Zeldovitch equation,

$$\frac{\partial c(N, t)}{\partial t} = \frac{\partial}{\partial N} \left[f_N \frac{\partial \beta \Delta\Omega(N)}{\partial N} c(N, t) + f_N \frac{\partial}{\partial N} c(N, t) \right], \quad (1.2)$$

where $c(N, t)$ is the concentration of clusters of size N per unit volume at time t . From this equation, we can derive the nucleation rate

$$J = f_{N_c} \sqrt{\frac{|\Delta\Omega''(N_c)|}{2\pi}} e^{-\beta\Delta\Omega(N_c)}, \quad (1.3)$$

where N_c is the size of the critical cluster and the double prime denotes the second derivative with respect to N . The attachment frequency is an input that cannot be deduced from this theory. Its expression depends on the transport processes involved in the nucleation. For colloids, we can assume that the dynamics is diffusion-limited and the attachment rate can be obtained by solving the diffusion equation.

At low supersaturation and for big clusters, CNT works relatively well. However, the macroscopic models used for quantities like the free energy barrier and attachment rates are heuristic and their input often has to be taken from experimental data rather than evaluated from basic principles.

Many developments to improve CNT exist in the literature and generally aim at a better estimation of the quantities that the theory takes as inputs [10]. One

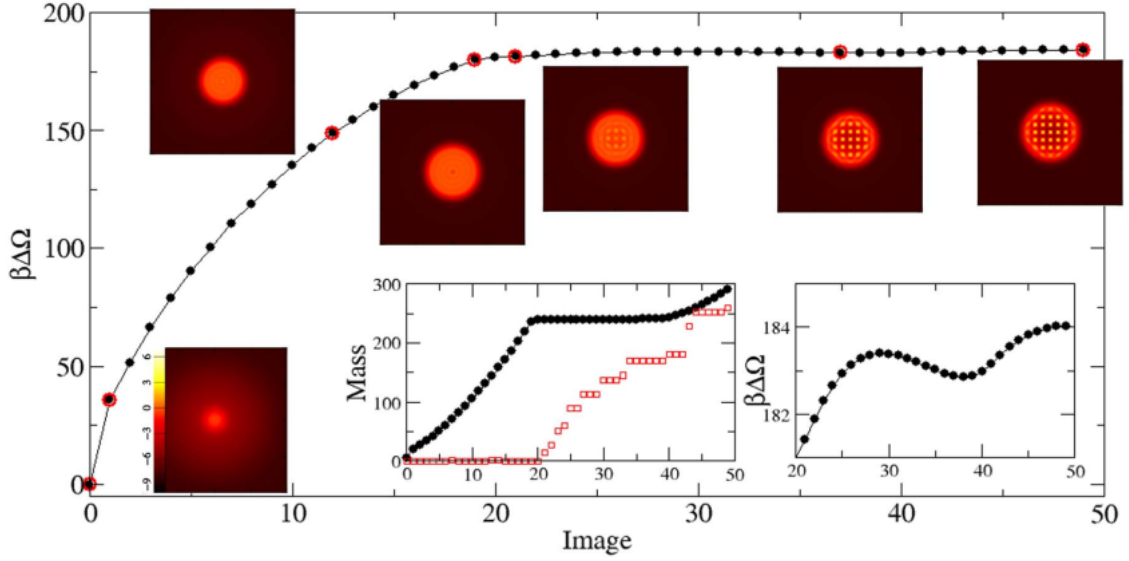


Figure 1.2 – Non classical nucleation pathway for crystallisation [11]. The image shows the evolution of the free energy along the reaction pathway, for a cluster of approximately 286 growth units. Nucleation starts with the accumulation of mass from a density fluctuation (black dots in the left inset). The crystalline order then appears in the droplet (the red dots in the left inset show the number of density peaks above the threshold $\rho\sigma^3 > 5$). A close look at the free energy curve shows a metastable intermediate state on the pathway (right inset).

way is to improve the description of the free energy barrier. For example, we can consider that the cluster has different properties from the final bulk phase, due to its finite size. An other way is to search for more accurate expressions of the attachment rates. However, these developments are still formulated within the paradigm of CNT. Moreover, the domain of validity of CNT is quite restricted and it is unable to describe many problems in current research, like large supersaturation and non-classical nucleation pathways. Finally, one of the most important example of nucleation – crystallisation – necessarily involves multiple order parameters (e.g. crystallinity and density) and such multi-parameter descriptions are difficult to formulate with the tools of CNT. For all these reasons, work has been started to study nucleation with a more fundamental description of energetics and of fluctuations.

This work comes along developments on an alternative to CNT called Mesoscopic Nucleation Theory (MeNT) [12]. MeNT is a combination of finite temperature classical DFT and fluctuating hydrodynamics. The DFT is included to describe cluster structure and energetics down to molecular length scales [13] and fluctuating hydrodynamics provides the basic description of fluctuations required. In MeNT, a system is described by local fields like the density, velocity and temperature that evolve according to stochastic differential equations. These equations result from the combination of mass conservation, momentum conservation (Navier-Stokes), a heat equation and a stochastic contribution.

Currently, the theory has only been developed in the over-damped limit, a sim-

plification where only the density field remains in the equations, and can thus only be applied to diffusion-limited nucleation, where heat transport is negligible. This is the case of macromolecules in solution, for which the bath acts like a thermostat. A remarkable feature of MeNT is that pathways deduced from this formalism still go through the critical cluster thus recovering a key element of the nucleation phenomenology. Furthermore, in the weak-noise limit of the diffusion-limited case, introducing the CNT assumptions leads to the recovery of the Zeldovitch equation thus showing that MeNT is a more fundamental theory of which CNT is a simple but valid approximation [12].

The application of diffusion-limited MeNT to the nucleation of a liquid droplet from the vapour of a simple fluid has led to the discovery of “non classical” pathways [11]. In the CNT picture, nucleation starts from a small cluster of the new phase with the size a few atoms and then grows in a stochastic process until it reaches the critical cluster. MeNT shows that instead, nucleation is a two-step process which begins with a density fluctuation over a large region of space. The excess of mass then aggregates into a smaller region and the density of the cluster increases. The result is a dense cluster which then grows the same way as in CNT.

For crystallisation in simple fluids, the application of MeNT shows a similar two-step non-classical pathway (see Fig. 1.2) with a metastable intermediate [11]. This is potentially a mechanism that would explain the metastability of pre-critical clusters that have been observed in many systems [5, 6, 7, 8]. In protein systems, such metastable precursors are potentially very important as they may help to control and improve the crystallisation process [14, 15]. For this reason, they are currently the subject of intense research, but their nature remains poorly understood. The present work is a first step towards applying MeNT and potentially understand these precursors’ nature and role in crystallisation.

1.3 Overview of this work

In this work, we prepare future applications of MeNT on protein crystallisation. The aim is to check if the DFT model currently in use is appropriate to reproduce the “colloid-like” phase diagram for a potential modelling the interaction between proteins¹. To fulfil this objective, we develop code to make phase diagrams from classical DFT computations, building upon a library written by Lutsko [16]. Our task is to write the minimisation of the DFT functional as well as the code to compute coexistence curves.

To guide code development, we used the Lennard-Jones potential, for which the diagram in our DFT model is already known from previous work by Lutsko [13].

¹We often use the term “colloids”, which is a generic term referring to nanoparticles in suspension in a solvent, like proteins.

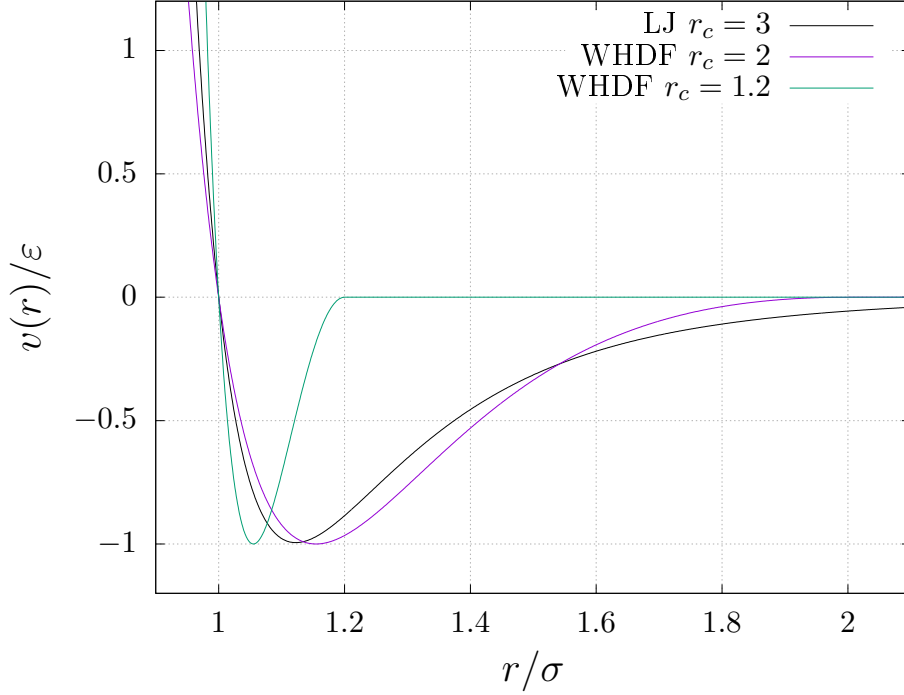


Figure 1.3 – Potentials used in this work. The WHDF potential can either model a simple fluid, like the Lennard-Jones potential does, or a colloid-like interaction, depending on the value of the cut-off parameter r_c . The values selected by the original authors are $r_c = 2$ for the simple fluid and $r_c = 1.2$ for colloids [17].

The formula of the Lennard-Jones potential is

$$v_{LJ}(r) = 4\varepsilon \left[\left(\frac{\sigma}{r} \right)^{12} - \left(\frac{\sigma}{r} \right)^6 \right], \quad (1.4)$$

where ε and σ are parameters defining the energy and length scales, respectively. We then focused our efforts on a new potential, given in an article of Wang et al. [17], that we will refer to as the WHDF potential,

$$v_{WHDF}(r) = 4\varepsilon\alpha \left[\left(\frac{\sigma}{r} \right)^2 - 1 \right] \left[\left(\frac{r_c}{r} \right)^2 - 1 \right], \quad (1.5)$$

where α is a normalisation factor to set the potential to -1 at its minimum. This potential was introduced as a computationally cheap alternative to the Lennard-Jones potential. It is designed to have a cut-off already implemented in the potential's formula, and to have a continuous derivative at the cut-off. These features make simulations easier by avoiding the need to truncate and shift it, as it is usually done with continuous potentials like Lennard-Jones. More importantly, the cut-off of the WHDF potential is a parameter that can be continuously changed to go from a potential very similar to Lennard-Jones, modelling simple fluids, to a colloid-like potential that we can use to describe proteins. Plots of the WHDF potential are shown on Fig. 1.3, next to the Lennard-Jones.

The document is structured as follows. First, we introduce elements of density functional theory. Then we present the DFT model that we use and explain how we minimise the DFT functional. Next, we show how we compute coexistence curves and show our results in phase diagrams. We continue by explaining how we perform specific computations to get the critical and triple points. We also discuss what we obtain for vacancy concentrations and compare them to simulation results. Last, we make DFT computations for the HCP solid configuration and talk about its relative stability with respect to the FCC configuration. The end of the document contains appendices to the main work. The first appendix explains our choices concerning units and notations. In particular, it contains lists of the symbols and abbreviations that we frequently use. The other appendices support specific chapters with additional information or calculations. The last one redirects to the source code that has been used in this work.

Chapter 2

Density functional theory

2.1 Introduction

Density Functional Theory (DFT) is a theoretical framework used to derive the equilibrium density in statistical mechanics. It relies on a one to one correspondence between external fields and densities, which allows one to write the grand canonical free energy as a functional of the density profile that is minimised by the equilibrium density. This reduces the problem of finding the equilibrium density of a physical system to a minimisation problem. However, the exact expression of the functional is unknown and the remaining problem is thus to find a suitable model for it.

In this chapter, we will quickly cover the basics of DFT and the state of the art concerning the aspects relevant to this work. We will start by recalling a few properties of the grand canonical ensemble, in which DFT is formulated. We will then show how the correspondence between fields and densities is derived and how this leads to a functional of the density. Next, we will discuss properties of the density functional that are important to the making of DFT models. In the following sections, we will review existing techniques to build free energy functional models for hard spheres and continuous potentials, focusing on the techniques we use in this work.

2.2 The grand canonical ensemble

The statistical ensemble in which DFT is formulated is the grand canonical ensemble. This is the ensemble in which the temperature, volume and chemical potential are constants. These quantities are control parameters that define the state of the ensemble, (kT, V, μ) . In the grand canonical ensemble, the density is a variable as it is not fixed by the control parameters, like it is in the canonical ensemble (kT, V, N) .

In the next sections, we will make use of a few properties of the grand canonical ensemble that we will expose here.

We first consider a classical system composed of N particles in an external potential ϕ , with an interaction potential v . The Hamiltonian contains a kinetic term \hat{K}_N , an interaction term between the particles \hat{V}_N and an interaction term \hat{U}_N coming from the external potential. Its expression is

$$\hat{H}_N = \underbrace{\sum_{i=1}^N \frac{\mathbf{p}_i^2}{2m_i}}_{\hat{K}_N} + \underbrace{\sum_{i < j} v(\mathbf{q}^N)}_{\hat{V}_N} + \underbrace{\sum_{i=1}^N \phi(\mathbf{q}_i)}_{\hat{U}_N}, \quad (2.1)$$

where \mathbf{q}_i denotes a particle's position and \mathbf{p}_i its momentum. A superscript N indicates a set of quantities for all N particles. Note that the contribution from the external potential ϕ can be written as a functional of ϕ using the density operator,

$$\hat{U}_N = \sum_{i=1}^N \phi(\mathbf{q}_i) = \int d\mathbf{r} \phi(\mathbf{r}) \sum_{i=1}^N \delta(\mathbf{r} - \mathbf{q}_i) = \int d\mathbf{r} \phi(\mathbf{r}) \hat{\rho}(\mathbf{r}). \quad (2.2)$$

The grand canonical ensemble is obtained by placing this system in equilibrium with thermal and chemical reservoirs so that it can exchange heat and particles with the reservoirs. The result is a system with fixed temperature and chemical potential, with a partition function

$$\Xi[\phi] = \sum_{N=0}^{\infty} \int d\mathbf{q}^N \int d\mathbf{p}^N \frac{1}{N! h^{DN}} e^{-\beta(\hat{H}_N - \mu N)} \quad (2.3)$$

and an equilibrium distribution that is

$$f(\mathbf{q}^N, \mathbf{p}^N, N, [\phi]) = \frac{1}{\Xi[\phi]} \frac{1}{N! h^{DN}} e^{-\beta(\hat{H}_N - \mu N)}. \quad (2.4)$$

The brackets denote a functional dependence on ϕ , and D is the dimension of the system. The free energy, called the grand potential, is related to the partition function by

$$\Omega[\phi] = -kT \ln \Xi[\phi]. \quad (2.5)$$

2.3 The fundamental theorem of DFT

Density functional theory takes its origins in the works of Hohenberg and Kohn [18], who formulated a variational principle to derive the density of an electron gas at

zero temperature from a density functional. This principle has been generalised for finite temperatures by Mermin [19], in a theorem that is now at the core of density functional theory. The theorem states that the grand potential of an electron gas in presence of an external one-body potential is the minimum of a unique functional of the density, which is minimised by the equilibrium density. In this section, we will show how we can derive this result for a classical system.

We start by defining a functional of the external field $\phi(\mathbf{r})$, using a reference field $\phi_0(\mathbf{r})$,

$$\Lambda[\phi; \phi_0] = \Omega[\phi_0] + k_B T \sum_{N=0}^{\infty} \int d\mathbf{q}^N \int d\mathbf{p}^N f_N[\phi] \ln \frac{f_N[\phi]}{f_N[\phi_0]}. \quad (2.6)$$

We can see that this functional gives the grand potential $\Omega[\phi_0]$ when evaluated at the field ϕ_0 . The grand potential is actually the minimum of this functional, as we can show that the relative entropy term is always positive. Indeed, using the inequality $\ln x \leq x - 1$,

$$\begin{aligned} & \sum_{N=0}^{\infty} \int d\mathbf{q}^N \int d\mathbf{p}^N f_N[\phi] \ln \frac{f_N[\phi]}{f_N[\phi_0]} \\ &= - \sum_{N=0}^{\infty} \int d\mathbf{q}^N \int d\mathbf{p}^N f_N[\phi] \ln \frac{f_N[\phi_0]}{f_N[\phi]} \\ &\geq - \sum_{N=0}^{\infty} \int d\mathbf{q}^N \int d\mathbf{p}^N f_N[\phi] \left(\frac{f_N[\phi_0]}{f_N[\phi]} - 1 \right) \\ &= - \sum_{N=0}^{\infty} \int d\mathbf{q}^N \int d\mathbf{p}^N (f_N[\phi_0] - f_N[\phi]) \\ &= 0. \end{aligned} \quad (2.7)$$

To prove that two external fields cannot lead to the same equilibrium density, we will need to rearrange the functional in order to have an explicit dependence on the local density. We do this by substituting the expression of the grand canonical equilibrium distribution:

$$\begin{aligned} \Lambda[\phi; \phi_0] &= \Omega[\phi_0] + k_B T \sum_{N=0}^{\infty} \int d\mathbf{q}^N \int d\mathbf{p}^N f_N[\phi] \cdots \\ &\quad \cdots \left(-\beta \sum_{i=1}^N \phi(\mathbf{q}_i) + \beta \sum_{i=1}^N \phi_0(\mathbf{q}_i) - \ln \Xi[\phi] + \ln \Xi[\phi_0] \right) \\ &= \Omega[\phi] + \sum_{N=0}^{\infty} \int d\mathbf{q}^N \int d\mathbf{p}^N f_N[\phi] \int d\mathbf{r} (\phi(\mathbf{r}) - \phi_0(\mathbf{r})) \hat{\rho}(\mathbf{r}) \\ &= \Omega[\phi] + \int d\mathbf{r} (\phi(\mathbf{r}) - \phi_0(\mathbf{r})) \rho(\mathbf{r}; [\phi]) \end{aligned} \quad (2.8)$$

where $\rho(\mathbf{r}; [\phi])$ denotes the local density under the external field ϕ . Now we can use the fact that $\Lambda[\phi, \phi_0]$ is minimum at ϕ_0 to get the following inequality for two distinct fields $\phi \neq \phi_0$:

$$\Omega[\phi_0] = \Lambda[\phi_0; \phi_0] < \Lambda[\phi; \phi_0] = \Omega[\phi] + \int d\mathbf{r} (\phi(\mathbf{r}) - \phi_0(\mathbf{r}))\rho(\mathbf{r}; [\phi]). \quad (2.9)$$

If two distinct fields could lead to the same density, we would have $\rho(\mathbf{r}; [\phi]) = \rho(\mathbf{r}; [\phi_0])$ and thus

$$\begin{aligned} \Omega[\phi_0] - \Omega[\phi] &< \int d\mathbf{r} (\phi(\mathbf{r}) - \phi_0(\mathbf{r}))\rho(\mathbf{r}; [\phi]) \\ &= - \int d\mathbf{r} (\phi_0(\mathbf{r}) - \phi(\mathbf{r}))\rho(\mathbf{r}; [\phi_0]) \\ &< \Omega[\phi_0] - \Omega[\phi]. \end{aligned} \quad (2.10)$$

However, this is a contradiction. We conclude that two distinct fields cannot lead to the same density, which implies a one-to-one correspondence between the fields and the densities:

$$\rho(\mathbf{r}; [\phi]) \leftrightarrow \phi(\mathbf{r}; [\rho]) \quad (2.11)$$

The correspondence between fields and densities is an important result as we can now define a density functional in an unambiguous manner:

$$\Omega[\rho; \phi_0] = \Lambda[\phi[\rho]; \phi_0] \quad (2.12)$$

Note that this functional is minimised by the equilibrium density $\rho(\mathbf{r}; [\phi_0])$ as $\Lambda[\phi[\rho]; \phi_0]$ is itself minimised by ϕ_0 . The value at the minimum is the grand potential $\Omega[\phi_0]$, therefore concluding the proof of the theorem.

2.4 Properties of the density functional

An important property of the density functional $\Omega[\rho; \phi_0]$ is that it can be separated into two terms,

$$\Omega[\rho; \phi_0] = F[\rho] + \int d\mathbf{r} (\phi_0(\mathbf{r}) - \mu)\rho(\mathbf{r}). \quad (2.13)$$

The dependence on the external field ϕ_0 is isolated in the second term and the first one is a functional that only depends on the density. This functional, $F[\rho]$, contains all the information on the interaction and is unique for the particle-particle interaction potential. Details on this property are given in appendix B.

The functional $F[\rho]$ obeys an important equation when evaluated at the equilibrium density. The fundamental theorem has taught us that the equilibrium density minimises the functional $\Omega[\rho; \phi_0]$. By applying this extremal principle on expression (2.13) we get a Euler-Lagrange equation for $F[\rho]$,

$$\frac{\delta\Omega[\rho; \phi_0]}{\delta\rho} = 0 \iff \frac{\delta F[\rho]}{\delta\rho} = \mu - \phi_0(\mathbf{r}). \quad (2.14)$$

This equation has a central role in DFT as it can be used to find an expression for the density functional $F[\rho]$. Given an expression for $\mu - \phi_0(\mathbf{r})$ in terms of the equilibrium density, we can integrate the Euler-Lagrange equation to find $F[\rho]$. This can be done exactly for simple systems whose partition function takes a simple form. Remarkable examples are the ideal gas, one particle in a small cavity or hard rods in one dimension. In appendix B, we show how to obtain the functional for the ideal gas.

In general, the system is not exactly solvable and approximations must be used for the density functional $F[\rho]$. In the next two sections, we will cover models that approximate the density functional for hard spheres, as well as for continuous potentials.

There are of course other methods to approximate the density functional $F[\rho]$. Many of them are based on a perturbation of the liquid state. The idea is to use an approximation of the direct correlation function to model the excess part of the density functional, $F_{ex}[\rho]$, as the two can be related by

$$\frac{\delta^2 \beta F_{ex}[\rho]}{\delta\rho(\mathbf{r}_1)\delta\rho(\mathbf{r}_2)} = -c_2(\mathbf{r}_1, \mathbf{r}_2; [\rho]), \quad (2.15)$$

where $c_2(\mathbf{r}_1, \mathbf{r}_2; [\rho])$ is the direct correlation function (DCF). This equation can be integrated twice to express $F[\rho]$ in terms of the DCF, using the liquid state as the reference state. This is convenient as the DCF has usually a simple structure and can be more easily approximated. The oldest example is the DFT model of Ramakrishnan and Yussouff,

$$\beta F_{ex}[\rho] - \beta F_{ex}(\bar{\rho}) = -\frac{1}{2} \int d\mathbf{r}_1 d\mathbf{r}_2 c_2(\mathbf{r}_{12}; \bar{\rho}) (\rho(\mathbf{r}_1) - \bar{\rho}) (\rho(\mathbf{r}_2) - \bar{\rho}), \quad (2.16)$$

where the DCF has been approximated by the DCF of the liquid state and $\bar{\rho}$ is the density of the liquid state, taken as the average density of the target profile $\rho(\mathbf{r})$.

2.5 Fundamental measure theory

Systems composed of hard spheres play an important role in statistical mechanics. They have one of the simplest interaction imaginable: a pair potential that takes an infinite value for distances under the hard sphere diameter and zero elsewhere. This means that hard sphere particles only interact by excluded volume effects. Despite their simplicity, hard sphere systems are not exactly solvable. The only exception is the one-dimensional system of "hard rods", for which an exact expression for the functional can be found:

$$\beta F[\rho] = \beta F_{id}[\rho] - \int \frac{\rho(x + d/2) + \rho(x - d/2)}{2} \ln \left(1 - \int_{-d/2}^{d/2} \rho(x + y) dy \right) dx, \quad (2.17)$$

where d is the hard rod length and $F_{id}[\rho]$ the ideal part of the functional. This exact result has an interesting structure: the density appears only as an average over the two extremities of the hard rod, centred in x , and as an average on the length of this same hard rod, respectively

$$\frac{\rho(x + d/2) + \rho(x - d/2)}{2} \quad \text{and} \quad \int_{-d/2}^{d/2} \rho(x + y) dy. \quad (2.18)$$

This inspired generalisations to higher dimensions, by writing the excess functional as an algebraic function Φ of simple density functionals $n_\alpha(\mathbf{r}, [\rho])$,

$$\beta F_{ex} = \int \Phi(\{n_\alpha(\mathbf{r}, [\rho])\}) d\mathbf{r}, \quad n_\alpha(\mathbf{r}, [\rho]) = \int w_\alpha(\mathbf{r} - \mathbf{r}') \rho(\mathbf{r}') d\mathbf{r}'. \quad (2.19)$$

The density functionals $n_\alpha(\mathbf{r}, [\rho])$, called the "fundamental measures", generalise density averages that appear in the hard rod result to higher dimensions. They take the form of a convolution between the density ρ and weight functions $w_\alpha(\mathbf{r})$.

The first DFT model of this sort has been given by Rosenfeld et al. [20]. It uses three density measures: a volume average,

$$\eta(\mathbf{r}) = \int \Theta \left(\frac{d}{2} - |\mathbf{r} - \mathbf{r}'| \right) \rho(\mathbf{r}') d\mathbf{r}' \quad (2.20)$$

that is the local packing fraction around point \mathbf{r} , a scalar surface average

$$s(\mathbf{r}) = \int \delta \left(\frac{d}{2} - |\mathbf{r} - \mathbf{r}'| \right) \rho(\mathbf{r}') d\mathbf{r}' \quad (2.21)$$

and a vectorial surface average,

$$\mathbf{v}(\mathbf{r}) = \int \widehat{\mathbf{r} - \mathbf{r}'} \delta \left(\frac{d}{2} - |\mathbf{r} - \mathbf{r}'| \right) \rho(\mathbf{r}') d\mathbf{r}', \quad (2.22)$$

where the hat $\widehat{}$ indicates a unit vector and d is the hard sphere diameter. The function Φ is derived in such a way that

1. the Euler-Lagrange equation (2.14) is satisfied,
2. its expression has the correct dimensions,
3. the density functional has the correct behaviour at low-density.

The resulting model is a sum of three terms, $\Phi = \Phi_1 + \Phi_2 + \Phi_3$, with

$$\Phi_1 = -\frac{s}{\pi d^2} \ln(1 - \eta), \quad \Phi_2 = \frac{1}{2\pi d} \frac{s^2 - v^2}{1 - \eta}, \quad \Phi_3 = \frac{1}{24\pi} \frac{s^3 - 3sv^2}{(1 - \eta)^2}. \quad (2.23)$$

A remarkable feature of this model is that in the uniform density limit, we recover exactly the Percus-Yevick equation of state for hard spheres. Also, Rosenfeld's functional successfully reproduces the behaviour of a hard sphere fluid near a wall. However, the functional fails to stabilise the solid because of the third term, Φ_3 , which is unbounded from below [13].

The success of Rosenfeld's model led to further developments to improve it. A first generalisation was made by Tarazona [21] by introducing a tensor density functional,

$$T_{\alpha\beta} = \int (\widehat{\mathbf{r} - \mathbf{r}'})_\alpha (\widehat{\mathbf{r} - \mathbf{r}'})_\beta \delta\left(\frac{d}{2} - |\mathbf{r} - \mathbf{r}'|\right) \rho(\mathbf{r}') d\mathbf{r}'. \quad (2.24)$$

Tarazona's contribution consists in a modification of the Φ_3 term,

$$\Phi_3 = \frac{3}{16\pi} \frac{\mathbf{v} \cdot \mathbf{T} \cdot \mathbf{v} - sv^2 + s \text{Tr}(\mathbf{T}^2) - \text{Tr}(\mathbf{T}^3)}{(1 - \eta)^2}, \quad (2.25)$$

resulting in a stabilisation of the solid phase when parametrised with gaussian profiles. However, the functional of Tarazona does not give very good results for the liquid-solid coexistence. This comes from the fact that, like the original Rosenfeld model, it is related to the Percus-Yevick equation of state which does not give an accurate description of the fluid at high densities.

A second generalisation was proposed by Roth et al. [22], giving a new functional called the "White Bear I" functional. They made empirical modifications to Tarazona's functional in order to recover the Carnahan-Starling equation of state [23] in the uniform density limit, which gives more accurate results at high densities. The White Bear I functional is

$$\begin{aligned} \Phi = & -\frac{s}{\pi d^2} \ln(1 - \eta) + \frac{1}{2\pi d} \frac{s^2 - v^2}{1 - \eta} \phi_1^{WBI}(\eta) \\ & + \frac{3}{16\pi} \frac{\mathbf{v} \cdot \mathbf{T} \cdot \mathbf{v} - sv^2 + s \text{Tr}(\mathbf{T}^2) - \text{Tr}(\mathbf{T}^3)}{(1 - \eta)^2} \phi_2^{WBI}(\eta) \end{aligned} \quad (2.26)$$

with

$$\phi_1^{WBI}(\eta) = 1 \quad \text{and} \quad \phi_2^{WBI}(\eta) = \frac{2}{3} \frac{\eta + (1 - \eta)^2 \ln(1 - \eta)}{\eta^2}. \quad (2.27)$$

Later, Roth et al. proposed another model with new White Bear functions, ϕ_1^{WBII} and ϕ_2^{WBII} , for a more accurate description of mixtures.

Despite their success at describing the solid phase, the tensor functionals of Tarazona and Roth are only stable for restricted profiles, e.g. a gaussian parametrisation of the solid. For many year, the study of the solid phase using a full minimisation of the density profile ¹ has been hampered by numerical instabilities. Recently, new evidence from Lutsko et al. [13] suggests that the tensor functionals are actually unbounded from below.

Bounded alternatives have been given by Rosenfeld [24], involving no tensor functionals, and can be obtained by modifying the numerator of the unbounded Φ_3 term. One example is the RSLT functional, where

$$\Phi_3 = \frac{1}{24\pi} \frac{s^3 [1 - v^2/s^2]^3}{(1 - \eta)^2}. \quad (2.28)$$

Like the original Rosenfeld model, these alternatives give the Percus-Yevick equation of state in the uniform limit. Following the recipe of Roth et al., the WBI functions can be introduced so that the function instead recovers the Carnahan-Starling equation of state in the uniform limit (see appendix B). The result is the modified RSLT functional (mRSLT),

$$\Phi = -\frac{s}{\pi d^2} \ln(1 - \eta) + \frac{1}{2\pi d} \frac{s^2 - v^2}{1 - \eta} + \frac{1}{24\pi} \frac{s^3 [1 - v^2/s^2]^3}{(1 - \eta)^2} \phi_2^{WBI}(\eta). \quad (2.29)$$

2.6 Continuous potentials

In this section we will review how continuous potential can be modelled using DFT. We will focus the discussion on potentials with a strong, short-range repulsion since these are the kind of potentials we are interested in, i.e. the Lennard-Jones and WHDF potentials.

The central idea is to model the repulsive core and the attractive tail separately, by approximating the repulsive core as a hard core interaction while treating the attractive tail as a correction of the hard core model. The resulting functional is a

¹By full minimisation we mean an unconstrained minimisation of the discretised density profile, by considering the density at each grid point as an independent parameter.

sum of three terms,

$$F[\rho] = F_{id}[\rho] + F_{hs}[\rho; d] + F_l[\rho], \quad (2.30)$$

where F_{id} is the ideal gas functional, $F_{hs}[\rho; d]$ is the excess hard sphere functional which depend on the effective hard sphere diameter that needs to be specified and $F_l[\rho]$ is the correction for the long-range attractive tail. The hard sphere functional is usually modelled using FMT and models for the tail will be discussed below.

There are several recipes to split the potential $v(r)$ into a repulsive $v_0(r)$ and an attractive $w(r)$ parts. The most common are the Barker–Henderson (BH) [25] and the Weeks–Chandler–Anderson (WCA) [26] divisions. The BH method consist in splitting the potential at the point where it crosses the zero,

$$\text{BH:} \quad \begin{cases} v_0(r) = v(r)\Theta(r_0 - r) \\ w(r) = v(r)\Theta(r - r_0) \end{cases} \quad \text{with } v(r_0) = 0. \quad (2.31)$$

In the WCA method the potential is split at its minimum instead, then shifted so that the repulsive part reaches zero at the split radius and the tail extends into the core. It gives

$$\text{WCA:} \quad \begin{cases} v_0(r) = (v(r) - v(r_{min}))\Theta(r_{min} - r) \\ w(r) = v(r_{min})\Theta(r_{min} - r) + v(r)\Theta(r - r_{min}) \end{cases}. \quad (2.32)$$

The BH division has the disadvantage of depending on an arbitrary choice for the zero of the potential. However, both methods usually lead to similar results [27].

To compute the hard sphere diameter, a simple prescription has been given by Barker and Henderson [25, 28],

$$d = \int_0^\infty (1 - \exp[-\beta v_0(r)]) dr. \quad (2.33)$$

This formula is obtained by minimising the deviations in the free energy between the effective hard core potential and $v_0(r)$. This involve estimations of the free energy difference based on an integration of the free energy functional and an expansion of the pair distribution function (PDF) of the hard sphere system around the hard sphere diameter. To get the BH formula, only the first functional derivative of the free energy is used for the integration and expansions of the PDF are truncated after the first term. This leaves room for improvement but using a more elaborate expression for the free energy results in an effective hard sphere diameter that is both dependent on the density and the hard sphere PDF. This makes the DFT model more complicated and a compromise must therefore be made between simplicity and accuracy.

Contributions from the long-range attractive tail can be modelled considering a

perturbative treatment of the direct correlation function (DCF). (2.15) shows that the DCF is related linearly to the free energy functional, which allows one to separate the DCF in a hard sphere term and a correction from the long-range interaction,

$$c_2(\mathbf{r}_1, \mathbf{r}_2; [\rho]) = c_2^{hs}(\mathbf{r}_1, \mathbf{r}_2; d, [\rho]) + \Delta c_2(\mathbf{r}_1, \mathbf{r}_2; d, [\rho]). \quad (2.34)$$

The hard sphere DCF c_2^{hs} is incorporated in the selected hard sphere model to describe the repulsive interaction and the remaining correction Δc_2 is treated in a new density functional $F_l[\rho]$, which can be constructed by integrating Δc_2 as explained at the end of section 2.4.

A simpler way to incorporate the long-range contribution in the density functional is to make use of a mean field approximation. It gives the functional

$$F_l[\rho] = \frac{1}{2} \iint \rho(\mathbf{r}_1) \rho(\mathbf{r}_2) w(|\mathbf{r}_1 - \mathbf{r}_2|) d\mathbf{r}_1 d\mathbf{r}_2. \quad (2.35)$$

This is actually equivalent to the integration of (2.15) using the DCF $\Delta c_2 = -\beta w(|\mathbf{r}_1 - \mathbf{r}_2|)$, which is independent of the density.

Chapter 3

DFT model: implementation and minimisation

3.1 The DFT model

In this work, the Helmholtz free energy functional is a sum of three terms,

$$\beta F[\rho] = \beta F_{id}[\rho] + \beta F_{hs}[\rho] + \beta F_{mf}[\rho]. \quad (3.1)$$

The first term is the ideal part of the free energy and the last two constitute the excess part, coming from the pair potential interaction. The excess part of the functional contains two terms because the repulsive and attractive parts of the potential are modelled separately, as explained in section 2.6. The split of the potential is done according to the WCA convention (2.32).

The expression of the ideal part is (see appendix B)

$$\beta F_{id}[\rho] = \int \{ \rho(\mathbf{r}) \ln(\rho(\mathbf{r})\sigma^3) - \rho(\mathbf{r}) \} d\mathbf{r}. \quad (3.2)$$

The argument of the logarithm is adimensionalised by multiplying the density with the length parameter σ of the potential, which is the unit length in practical computations. The choice of the length scale is equivalent to choosing the zero of the chemical potential. The conversion from our chemical potential μ to the one that we get by choosing the thermal length $\Lambda = h/(2\pi mkT)^{1/2}$ as the reference length scale is

$$\beta\mu_\Lambda = \beta\mu + 3 \ln(\Lambda/\sigma). \quad (3.3)$$

The repulsive part of the potential is modelled as an effective hard sphere interaction. The hard sphere diameter is computed according to the BH convention (2.33).

The model selected for the hard sphere interaction is the modified RSLT model (see section 2.5). The corresponding term is

$$\beta F_{hs}[\rho] = \int \Phi(\eta, s, \mathbf{v}) \, d\mathbf{r}, \quad (3.4)$$

$$\Phi(\eta, s, \mathbf{v}) = -\frac{s}{\pi d^2} \ln(1 - \eta) + \frac{1}{2\pi d} \frac{s^2 - v^2}{1 - \eta} + \frac{1}{24\pi} \frac{s^3 [1 - v^2/s^2]^3}{(1 - \eta)^2} \phi_2^{WBI}(\eta). \quad (3.5)$$

The last term takes into account the attractive part of the potential using a mean-field model,

$$\beta F_{mf} = \frac{1}{2} \iint \beta w(|\mathbf{r} - \mathbf{r}'|) \rho(\mathbf{r}) \rho(\mathbf{r}') \, d\mathbf{r} \, d\mathbf{r}'. \quad (3.6)$$

As we are focused on the study of homogeneous phases, we do not consider any external field. The grand canonical free energy functional is thus

$$\Omega[\rho] = F[\rho] - \int \mu \rho(\mathbf{r}) \, d\mathbf{r}. \quad (3.7)$$

This is the functional that needs to be minimised according to density functional theory. However, the quantity that we are most interested in is actually the grand canonical free energy per unit volume,

$$\beta \omega = \beta \Omega/V = \beta F_{id}/V + \beta F_{hs}/V + \beta F_{mf}/V - \beta \mu. \quad (3.8)$$

There are several reasons for that. First, the volume is fixed in the grand canonical ensemble, so dividing by it does not change the nature of the problem¹. Second, the resulting quantity is an intensive quantity, which makes it more meaningful². A third reason has to do with the way the solid phase is modelled, but that will be explained a bit further in the text (see section 3.7).

3.2 Evaluation of the DFT functional

The implementation of the DFT model was already available in the classical DFT library written by Lutsko [16]. This library is the base on which we built the code for this work. It contains the necessary tools to evaluate the free energy functional from a given density profile. We will not detail the inner workings of this library

¹The same is true for the temperature, this is why we can also multiply by $\beta = 1/kT$.

²Again true for the temperature, $\beta \omega$ is the free energy in the thermal energy unit kT .

here. The corresponding entry in the bibliography contains a link to the GitHub page that hosts the source code.

We will however mention a point that is relevant for this work. In the evaluation of the free energy functional, there are several spherical integrations that must be made. This was initially performed numerically using pre-compiled weights associated to points on the sphere generated in order to not bias the integration in any direction. The use of these weights was time-consuming and caused a few problems that we will discuss further in the text (see sections 3.6, 7.1 and appendix C). In parallel to this work, the library was updated by Lutsko to perform the spherical integration analytically. These changes were incorporated in this work's code too but many results were already obtained using the pre-compiled weights. For consistency, the data presented here is therefore computed using the pre-compiled weights exclusively.

3.3 The case of a uniform density

For fluid phases with no external potentials, the density is uniform because of the invariance under continuous translations. In that case, the expression of the free energy functional is greatly simplified as it reduces to an ordinary function of one variable, the uniform density $\rho(\mathbf{r}) = \rho$.

The expressions of the ideal and mean field terms are easy to find, becoming

$$\beta F_{id} = \int \{\rho \ln \rho - \rho\} d\mathbf{r} = \{\rho \ln \rho - \rho\} V, \quad (3.9)$$

$$\beta F_{mf} = \frac{1}{2} \iint \rho^2 \beta w(|\mathbf{r} - \mathbf{r}'|) d\mathbf{r} d\mathbf{r}' = \frac{1}{2} \rho^2 \int \beta w(\mathbf{r}') d\mathbf{r}' \int d\mathbf{r} \equiv a \rho^2 V, \quad (3.10)$$

where V is the volume of the system. We introduced a parameter, usually called the Van der Waals parameter, that alone characterises the mean field interaction,

$$a = \frac{1}{2} \int \beta w(\mathbf{r}) d\mathbf{r}. \quad (3.11)$$

The expression of the hard core term $\beta F_{hs}[\rho]$ is less obvious. In the uniform density limit, the density measures of FMT reduce to $\eta = \frac{\pi}{6} d^3 \rho$, $s = \pi d^2 \rho$, $\mathbf{v} = 0$.

The mRSLT functional thus becomes

$$\begin{aligned}
\Phi(\eta, s, \mathbf{v}) &= -\rho \ln(1 - \eta) + \frac{1}{2} \frac{\pi d^3 \rho^2}{(1 - \eta)} + \frac{1}{36} \frac{\pi^2 d^6 \rho^3}{(1 - \eta)^2} \frac{\eta + (1 - \eta)^2 \ln(1 - \eta)}{\eta^2}, \\
&= -\rho \ln(1 - \eta) + \frac{1}{2} \frac{\pi d^3 \rho^2}{(1 - \eta)} + \frac{1}{36} \pi^2 d^6 \rho^3 \left[\frac{1}{\eta(1 - \eta)^2} + \frac{1}{\eta^2} \ln(1 - \eta) \right], \\
&= -\rho \ln(1 - \eta) + \frac{3\eta\rho}{(1 - \eta)} + \frac{\eta\rho}{(1 - \eta)^2} + \rho \ln(1 - \eta), \\
&= \frac{3\eta\rho(1 - \eta) + \eta\rho}{(1 - \eta)^2}, \\
&= \rho \frac{\eta(4 - 3\eta)}{(1 - \eta)^2},
\end{aligned} \tag{3.12}$$

and so

$$\beta F_{hs}[\rho] = \int \Phi(\eta, s, \mathbf{v}) d\mathbf{r} = \rho V \frac{\eta(4 - 3\eta)}{(1 - \eta)^2}. \tag{3.13}$$

Using the expression we just derived above, we find the expression for the grand canonical free energy per unit volume and its derivative,

$$\boxed{\beta\omega(\rho) = \rho \ln \rho - \rho + \rho \frac{\eta(4 - 3\eta)}{(1 - \eta)^2} + a\rho^2 - \beta\mu\rho} \tag{3.14}$$

and

$$\boxed{\beta \frac{\partial\omega(\rho)}{\partial\rho} = \ln \rho + \frac{\eta(3\eta^2 - 9\eta + 8)}{(1 - \eta)^3} + 2a\rho - \beta\mu.} \tag{3.15}$$

3.4 Minimisation for fluid phases

As the uniform free energy is a one-variable function, the equilibrium density can simply be found by solving $\beta \frac{\partial\omega(\rho)}{\partial\rho} = 0$. However, due to the presence of a logarithm, this equation must be solved numerically. This task is a root-finding problem that we solve using the bisection method, implemented in the GSL library [29]. More sophisticated algorithms do indeed exist but the simple bisection algorithm works well enough in this case. Care must be taken however as multiple roots can exist for this equation. If the fluid is under the critical point there are three roots: two for the vapour and liquid densities plus one in between, corresponding to an unstable solution (see Fig. 3.1). A root-bracketing algorithm like the bisection algorithm must be given an initial search interval containing only one root. A way to choose such intervals is to use the spinodal densities.

Spinodal densities correspond to densities for which the second derivative of the free energy equals zero. Physically, they delimit the region where metastable vapour or liquid phases are possible. The second derivative is given by

$$\beta \frac{\partial^2 \omega(\rho)}{\partial \rho^2} = \frac{1}{\rho} + \frac{\eta}{\rho} \frac{8 - 2\eta}{(1 - \eta)^4} + 2a. \quad (3.16)$$

The problem of finding the roots of the second derivative is easier because its expression does not contain any logarithm. It reduces to finding the roots of a 5th-order polynomial in η :

$$0 = 2\tilde{a}\eta^5 + (1 - 8\tilde{a})\eta^4 + (-4 + 12\tilde{a})\eta^3 + (4 - 8\tilde{a})\eta^2 + (4 + 2\tilde{a})\eta + 1, \quad (3.17)$$

where $\tilde{a} = a \left[\frac{4\pi}{3} \left(\frac{d_{hs}}{2} \right)^2 \right]^{-1}$. We use a polynomial solver from the GSL library to find the packing fractions η and by extension, the spinodal densities. Despite being of 5th order, this polynomial should only have 0 or 2 real positive solutions, whether the temperature is above or under the critical temperature. The case of being exactly at the critical temperature would lead to one real positive solution but is unlikely to be encountered using floating-point numbers.

With the knowledge of the spinodal densities, we are now better equipped to tackle the problem of finding densities that minimise the free energy. Ignoring particular cases like being exactly at the critical temperature or on a spinodal curve, we encounter four possible behaviours for $\frac{\partial \omega}{\partial \rho}$ (see Fig. 3.1). These four cases can be identified from the sign of $\frac{\partial \omega}{\partial \rho}$ at spinodal densities $\rho_{s,1}$, $\rho_{s,2}$ and from the temperature relative to the critical temperature T_c .

1. $T > T_c$. There is a single root, corresponding to the supercritical fluid. There is no spinodal densities as we are above the critical temperature.
2. $T < T_c$, $\frac{\partial \omega}{\partial \rho} \big|_{\rho_{s,1}} > 0$, $\frac{\partial \omega}{\partial \rho} \big|_{\rho_{s,2}} > 0$. There is a single root, corresponding to the vapour phase. The liquid phase does not exist for such densities, below its associated spinodal curve.
3. $T < T_c$, $\frac{\partial \omega}{\partial \rho} \big|_{\rho_{s,1}} > 0$, $\frac{\partial \omega}{\partial \rho} \big|_{\rho_{s,2}} < 0$. There are three roots. The smaller one corresponds to the vapour phase and the higher one to the liquid phase. The intermediate root does not match any physical state, we can see that it is an unstable solution from the negative slope of $\frac{\partial \omega}{\partial \rho}$, i.e. $\frac{\partial^2 \omega}{\partial \rho^2} < 0$.
4. $T < T_c$, $\frac{\partial \omega}{\partial \rho} \big|_{\rho_{s,1}} < 0$, $\frac{\partial \omega}{\partial \rho} \big|_{\rho_{s,2}} < 0$. There is a single root, corresponding to the liquid phase. The vapour phase does not exist for such densities, above its associated spinodal curve.

In the first case, the interval chosen for the bisection algorithm spans from an arbitrary low density ρ_{min} to an arbitrary high one ρ_{max} . We must choose these densities with enough margin to find the physical solution in between. In the other

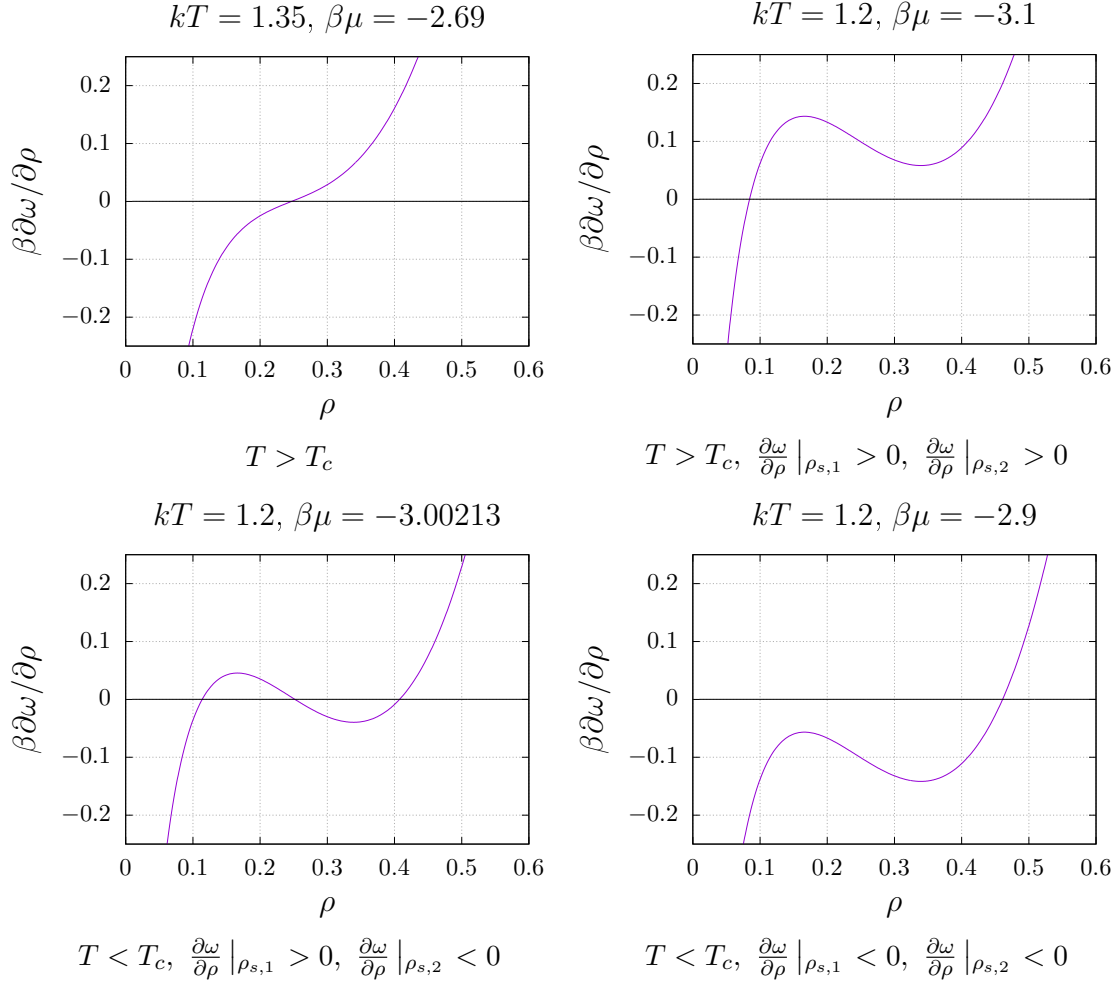


Figure 3.1 – The four cases encountered for the first free energy derivative. Spinodal densities are located where the slope is zero. These graphs have been generated using the Lennard-Jones potential with a cut-off $r_c = 3$.

cases, we search between ρ_{min} to the lowest spinodal density for the vapour and from the higher spinodal density to ρ_{max} for the liquid. The bisection algorithm stops when it reaches a relative precision of 10^{-8} .

3.5 Parametrisation of the solid density

In the solid, the density is not invariant under translation. Instead, it peaks in an orderly fashion around precise (relative) positions, or "sites" corresponding to particular lattice. In this work we consider crystalline solids structured in a FCC lattice (face-centred cubic, see Fig. 3.2). The FCC lattice is usually the most stable configuration and its cubic structure is easy to implement. For the Lennard-Jones potential, simulations show that the FCC phase is the most stable phase, except at low temperatures where the stable phase is the HCP configuration (hexagonal closed packed) [30]. For the WHDF potential, the FCC lattice is also the most stable when we consider a cut-off $r_c = 1.2$ (colloid-like) [17]. However, for a cut-off $r_c = 2$, the most stable configuration is HCP. However, in any of these cases, we do not expect a large difference in stability, because the two structures only differ at the second neighbour³. We discuss results for the HCP lattice in chapter 8, where we also compare the relative stability of the FCC and HCP configuration.

We model the density profile as a sum of gaussian curves centred on the lattice sites. This parametrisation of the solid density is usually a good approximation and is very common in the DFT literature, as it was the state of the art until the 2000s. We can motivate this choice considering the fact that near a lattice site the potential can be locally approximated by a parabola (this is the assumption made in the Einstein model for the solid). If we consider a particle at one lattice site in an effective potential generated by other particles, the density of the particle will behave like the exponential of the effective potential. In this approximation, the density is shaped as the exponential of a parabola, i.e. a gaussian curve. This suggests that the gaussian profile is a reasonable guess for the density near a lattice site.

In the gaussian parametrisation, the density is given by

$$\rho(\mathbf{r}) = \rho_0 \sum_{\mathbf{R} \in \mathcal{B}} \left(\frac{\alpha}{\pi} \right)^{\frac{3}{2}} e^{-\alpha |\mathbf{r} - \mathbf{R}|^2}, \quad (3.18)$$

where \mathcal{B} is the set of lattice sites in the lattice, α a parameter controlling the width of the gaussians and ρ_0 a parameter controlling the amplitude of the gaussian curves. To describe a perfect crystal, ρ_0 must be set to one. This ensures that the density is normalised such as the number of particles and the number of lattice sites are the same. To take lattice vacancies into account we set $\rho_0 = 1 - c_{vac}$ where c_{vac} is the

³See chapter 8 for more details on the differences between FCC and HCP

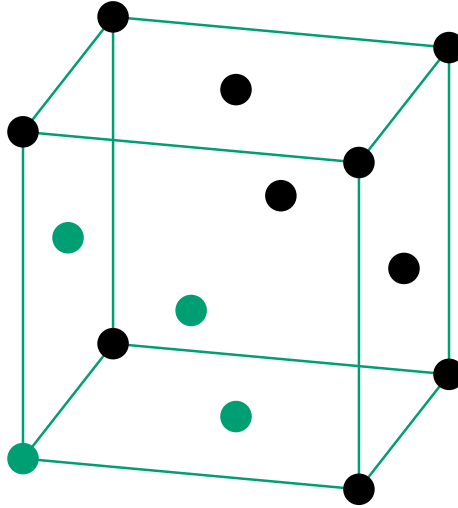


Figure 3.2 – The FCC structure. The blue lines highlight the borders of the cubic cell used for computations. The blue dots are the lattice sites which constitute the basis of the cubic cell.

average fraction of empty lattice sites in the solid, most often called the vacancy concentration. We initialise the density considering only contributions from the sites at a distance smaller than half the lattice constant. Usually, we encounter lattice constants of about $a_{latt} \approx 1.5$ and α ranging from 50 to 1000. With $\alpha = 50$, the contribution to the density profile is already by far negligible. At the shortest distance, $a_{latt}/2$, it is about

$$\Delta\rho \approx \left(\frac{50}{\pi}\right)^{\frac{3}{2}} \exp\left(-50 \times (1.5/2)^2\right) \approx 100 \times \exp\left(-50 \times (0.75)^2\right) \approx 6 \times 10^{-11}. \quad (3.19)$$

In actual computations, the density is discretised on a grid with a finite spacing $\delta_x = \delta_y = \delta_z$. The volume filled by this grid is chosen to match the conventional cubic cell for the FCC lattice, with periodic boundary conditions. Because the grid spacing δ_x is kept constant and because we must obey periodic boundary conditions, we are restricted to a discrete set of lattice constants given by the multiples of the grid spacing. With N_{grid} being the number of grid points that fill the side of the cubic grid, the lattice constants are $a_{latt} = N_{grid} \delta_x$.

For practical reasons, we use the same grid spacing in all our computations. This choice is made for consistency between the many quantities that are computed on a discretisation grid. For example, the fluid calculations use the effective hard sphere diameter and the Van der Waals interaction parameter (see section 3.3) that are also computed with a spatial integration. This is a minor concern for the determination of coexistence curve, but if we want to use our results to later compute interfaces between two phases, like a vapour-liquid interface, we will have to use one grid for the two phases. It is therefore appropriate that our reference data is computed using

δ_x	0.05	0.025	0.0125	0.00625
$\beta\omega$	0.251	0.0997	0.0604	0.0509

Table 3.1 – Evolution of the free energy with the grid spacing, for $kT = 0.6$, $\beta\mu = -7.6$, $N_{grid} = 128 \times 0.0125/\delta_x$, $c_{vac} = 2.4406 \times 10^{-5}$ and $\alpha = 148.42$. The potential is Lennard-Jones with a cut-off $r_c = 3$.

always the same grid spacing.

The choice of the grid spacing is a trade-off between accuracy and resource consumption. We choose the value $\delta_x = 0.0125$, which gives a reasonable accuracy. Table 3.1 shows how the value of the free energy changes with the grid spacing. Later in this work, we faced a few problems related to the grid spacing. They are discussed in appendix C.

To summarise, our model for the solid density profile involves three parameters. Two of them are parameters of the gaussian curves that we place at each lattice site : the vacancy concentration c_{vac} and the width parameter α . The third, N_{grid} , controls the FCC lattice constant. The DFT functional needs to be minimised with respect to each one of these parameters. The minimisation procedure is explained in the next two sections. It starts with c_{vac} and α and finishes with a minimisation over N_{grid} .

3.6 Minimisation over gaussian profiles

The first step in the minimisation of the density free energy functional is to minimise with respect to c_{vac} and α , keeping N_{grid} constant. This means keeping the same discretisation grid and changing the density initialisation with the gaussian profiles in a controlled manner, until we reach a minimum of the free energy functional.

The typical landscape of the free energy functional is shown on Fig. 3.3, for a given number of grid points. Naturally, near coexistence ⁴, we expect two minima corresponding to the uniform phase ($\alpha = 0$) and the solid phase. Nothing ensures that there is not more than one minimum for the solid, but the computations always show a single solid minimum in the region of the parameter space that we explored. Fig. 3.3 shows that in our DFT computations, the fluid phase minimum is not exactly at $\alpha = 0$. This is an expected behaviour as the density initialisation is done considering only a few lattice points. For low α , the gaussian profiles extends far beyond the computational cubic cell. The computations are thus incorrect because the number of particle is underestimated. It is not a problem however as we are

⁴Of course, we can expect that far from coexistence either the fluid or the solid phase becomes unstable, leaving only one minimum for the stable phase.

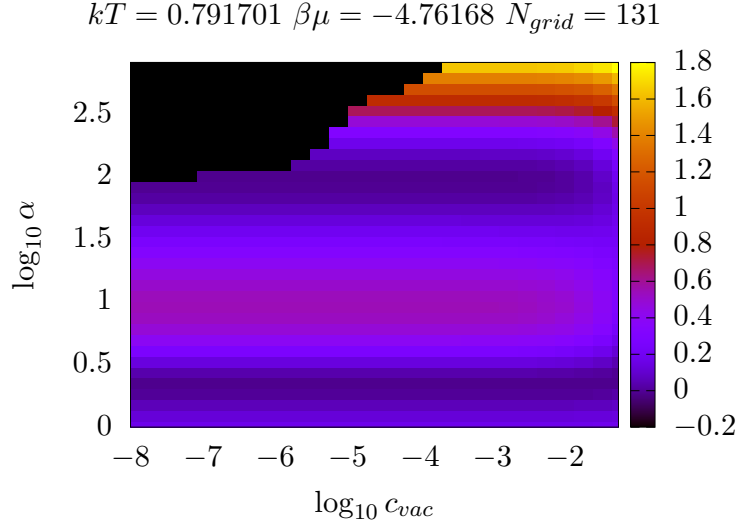


Figure 3.3 – Typical landscape of free energy functional near the triple point of the LJ potential, using a cut-off $r_c = 3$. The black colour represents unsuccessful computations, outlining the region where this implementation of the functional diverges.

only interested in the solid phase minimum which is located at much larger values of α . In all computations we have made, α took values between 50 and 1000 at the minimum of the DFT functional.

We perform the minimisation with respect to c_{vac} and α using the GSL implementation of the Nelder-Mead algorithm [29]. This is a multidimensional minimisation algorithm that only requires to evaluate the function to minimise, not its derivative. It seemed adequate for this problem and works fine. More efficient algorithms probably exist but efficiency is not our primary concern. We initialise the algorithm with a value of α high enough to avoid converging towards the uniform phase minimum. We choose⁵ $\alpha = 300$ and $c_{vac} = 1 \times 10^{-3}$ as a starting position. We slightly modify the algorithm to detect the crossing of given boundaries, usually at $\alpha = 20$, $\alpha = 10000$, $c_{vac} = 1 \times 10^{-8}$ and $c_{vac} = 1 \times 10^{-1}$, to report an error if the algorithm explore an unexpected region. We stop the algorithm when the simplex size drops below 2.5×10^{-3} . However, no such error was reported as the minimisation correctly finds the solid minima.

At high values of α and low values of c_{vac} , Fig. 3.3 shows a black region which indicates that the computations fail. This is caused by the use of the pre-compiled weights to perform spherical integrations numerically during the evaluation of the free energy functional (see section 3.2). The problem is that when the density profile is too sharply peaked around lattice sites, there is not enough points available in the weights file to compute the integral accurately. This results in a divergence in the hard sphere term of the free energy functional, more precisely the Φ_3 term of

⁵The starting positions and stopping criterion are coded as options, but for the results presented further in the text, we used these values.

the mRSLT model,

$$\Phi_3 = \frac{1}{24\pi} \frac{s^3[1 - v^2/s^2]^3}{(1 - \eta)^2}. \quad (3.20)$$

If the density peak is too sharp, the packing fraction η becomes very close to 1. With an imprecise computation of η , it can result in values too close to 1 or even higher. A value $\eta > 1$ is physically impossible in the effective hard-sphere model, because hard spheres cannot overlap. In this case, the computation of this term is aborted and returns an error. We must underline the fact that this divergence is caused by our implementation and is not an intrinsic behaviour of the free energy functional. In appendix C, we show the free energy landscape for several temperatures as well as for other potentials. In particular, we show that the analytic evaluation of the spherical integrals developed by Lutsko⁶ does not have this divergence problem.

The free energy functional still presents a minimum close to the frontier of the region of divergence. Although this is not the true minimum of the functional, but only the minimum of the implementation using the pre-compiled weights, we still return it at the end of the minimisation process. That is because the dependence of the free energy on the vacancy concentration is very weak in this region. Therefore, the free energy at this minimum is already very close to the exact one. This divergence problem is thus not a big deal for the computation of most physical properties. We should however be careful when it comes to vacancy concentrations because in this case the reported value can be very far from the actual one.

To avoid failures when the algorithm enters the divergence region during the minimisation, we artificially set the free energy to a high number (we choose 1×10^8) times $(1 - c_{vac})$. We do this in order to drive the algorithm towards higher values of c_{vac} , thus escaping the problematic region. This ensures that the minimum, which is very close to the region where the functional diverges, can be found every time.

Last, we can mention that the minimisation over vacancy concentrations can be omitted, depending on the purpose of the calculation. For phase diagrams, the computation we conducted showed that the difference with and without the minimisation over c_{vac} was not even visible when the coexistence curves were plotted on a graph. We still proceed to minimise over c_{vac} because we want to report the vacancy concentration at equilibrium.

3.7 Minimisation over lattice sizes

After having minimised over the gaussian profile parameters c_{vac} and α , we are left with the minimisation over the number of grid points N_{grid} . This step is actually a minimisation over the lattice constant $a_{latt} = N_{grid} \delta_x$ but, as we explained in section

⁶cf. discussion in section 3.2

3.5, our choice of keeping the grid spacing δ_x constant constrains us to work with discrete values of the lattice constant. For this reason, we do not seek the value of N_{grid} that minimises the functional but rather the floating-point value of N_{grid} , which corresponds to the actual lattice constant that minimises the functional.

At this stage there is another subtlety that must be reported. Until now, because we work in the grand canonical ensemble, the volume of the system did not matter for the minimisation, as dividing the functional by a constant factor does not change the position of the minimum. However, it matters now. The fact that we minimise over a parameter that defines the volume of the system implies that we are actually comparing different systems. To be consistent in our minimisation, we need to consider the free energy per unit $\beta\omega[\rho]$ volume rather than the total free energy $\beta\Omega[\rho]$. This choice is adequate because the free energy per unit volume is an intensive quantity and so does not depend on the system size.

That being said, we can now explain the minimisation procedure. It starts with an arbitrary value of N_{grid} for which we evaluate the free energy functional. We then evaluate the functional at neighbour values and follow the slope until we reach the minimum. At this point, we have the integer value of N_{grid} that minimises the free energy functional. The next step is to interpolate the free energy profile using three data points near the (integer) minimum. Our interpolation method is simple: we use these three data points to define a parabola. We then return the minimum of the parabola as the (floating-point) value of N_{grid} corresponding to the lattice constant that minimises the free energy functional. Once the minimum (floating-point) value of N_{grid} is found, we evaluate all the other quantities at the minimum using the same quadratic interpolation method. At this point, the quantities that we are tracking are the free energy per unit volume $\beta\omega$, the average solid density ρ_S , the vacancy concentration c_{vac} and the gaussian width parameter α . Now that we have the (floating-point) value of N_{grid} at the minimum, we can add it to the list. This completes the description of the solid state at given temperature and chemical potential.

Chapter 4

Coexistence curves

4.1 Generalities

In this chapter, we explain how we compute the phase coexistence curves. In the previous chapter, we presented the DFT model and explained how the minimisation of the DFT functional was performed. At this point, we have the tools in hand to compute the physical properties at given thermodynamic conditions, i.e. for a given set of the control variables (kT, V, μ) in the grand canonical ensemble. Now, the problem that remains is to use these computational techniques to find the phase coexistence curves. This is what we explain in this chapter. The computed curves are presented and discussed in the next chapter on phase diagrams.

Coexistence between two phases occurs under particular thermodynamic conditions. It happens when a system has the same free energy whether it has the configuration of phase 1 or phase 2. We can derive explicit conditions by considering a system made of two subsystems, one for each phase. In the grand canonical ensemble, the free energy is $\Omega = -pV$, where p is the pressure and V is the volume of the system. The total free energy is thus

$$\Omega_{1+2} = -p_1 V_1 - p_2 V_2. \quad (4.1)$$

The relative stability of the two phases can be checked by considering variations of the volume of the two phases. If the volume of phase 1 grows by dV_1 , the volume of the other will change by $dV_2 = -dV_1$, as the total volume is constant. The associated change in the total free energy is

$$d\Omega_{1+2} = -p_1 dV_1 - p_2 dV_2 = -(p_1 - p_2) dV_1. \quad (4.2)$$

If the two phases are in equilibrium with one another, this infinitesimal variation of the total free energy must be equal to zero. We deduce that in the grand canonical ensemble, a necessary condition for phase coexistence is an equilibration of the

pressure in the two phases. It is also sufficient, as the volume is the only extensive parameter in this ensemble. We thus have

$$d\Omega_{1+2} = 0 \iff p_1 = p_2. \quad (4.3)$$

The same reasoning could have been formulated with the free energy per unit volume, $\omega = -p$, which is just minus the pressure. In practice, we use the condition of equilibration of the free energies per unit volume, in reduced energy units:

$$\boxed{\beta\omega_1 = \beta\omega_2.} \quad (4.4)$$

To reformulate using more specific terms, our problem is to find the values of (kT, μ) for which the free energy per unit volume $\beta\omega$ of the two phases are the same. We will proceed by finding the coexistence point at fixed temperature and then repeat for a range of temperatures in order to get a coexistence curve.

We will consider the coexistence between vapour and liquid phases as well as the coexistence between the fluid phases and the solid. For simple fluids, i.e. the LJ and WHDF $r_c = 2$ potentials, vapour-solid and liquid-solid coexistences will be treated separately, though following the same procedure. In colloids (WHDF $r_c = 1.2$), we will see that the solid can coexist only with the vapour and supercritical fluid. For the latter, there is no ambiguity in the nature of the fluid phase and we will simply refer to it with the generic term "fluid".

4.2 The vapour-liquid coexistence

In the case of the vapour-liquid coexistence, we can simplify the problem of finding the coexistence even further. In the default procedure, we start with an arbitrary value of the chemical potential μ , then minimise the free energy functional to find the equilibrium densities. As detailed in section 3.4, this is a general root-finding problem for $\beta\partial\omega/\partial\rho$ that leads to one or two stable minima, corresponding either to the vapour or the liquid phase. We then compute the free energy associated with each density and compare them. These steps are reiterated until the difference of the two free energies is sufficiently close to zero. So, this procedure involves three root-finding problems: two to find the densities ρ_V and ρ_L of the vapour and liquid phases and one to find the value of the chemical potential that cancels the free energy difference $\beta\omega_V - \beta\omega_L$. Rather than doing so, we manipulate the simple expression of the uniform free energy functional to have a procedure that requires only one general root-finding problem and solving a simple polynomial.

The uniform free energy functional and its derivative are simple functions of one

variable that we derived in section 3.3:

$$\beta\omega(\rho) = \rho \ln \rho - \rho + \rho \frac{\eta(4-3\eta)}{(1-\eta)^2} + a\rho^2 - \beta\mu\rho, \quad (4.5)$$

$$\beta \frac{\partial\omega(\rho)}{\partial\rho} = \ln \rho + \frac{\eta(3\eta^2 - 9\eta + 8)}{(1-\eta)^3} + 2a\rho - \beta\mu. \quad (4.6)$$

we can eliminate the logarithm term as well as the chemical potential by considering the combination

$$\boxed{\beta\omega(\rho) - \rho\beta \frac{\partial\omega(\rho)}{\partial\rho} = \rho \frac{\eta^3 - \eta^2 - \eta - 1}{(1-\eta)^3} - a\rho^2.} \quad (4.7)$$

This combination is actually an expression for the free energy, as the derivative $\frac{\partial\omega(\rho)}{\partial\rho}$ is always zero¹. At coexistence, the free energies of the vapour and liquid phase are the same, $\beta\omega_V = \beta\omega_L$. It means that (4.7) has the same parameter for both the vapour and liquid densities and both densities are thus solution of the same equation.

This gives a procedure to find the coexistence. We start from an arbitrary value of the vapour density, ρ_V , evaluate the free energy $\beta\omega_V$ and find the corresponding value of the liquid density ρ_L by solving (4.7) for the density. For both densities, the free energy is the same by construction but the associated chemical potentials are different. We find the coexistence densities by iterating these steps until both chemical potentials are the same. This leaves only one root-finding problem, finding the vapour density that cancels the chemical potential difference $\mu_V - \mu_L$. We solve it using the bisection algorithm from the GSL library [29]. We iterate until we reach a relative precision of 10^{-8} . Solving (4.7) is only a polynomial problem, as we got rid of the logarithm term.

We can explicitly put (4.7) in polynomial form by introducing $\tilde{\omega} = \beta\omega\eta/\rho$ and $\tilde{a} = a\rho/\eta$. We will write a polynomial for the packing fraction η , from which we can recover the density using the relation

$$\eta = \frac{\pi}{6} d_{hs}^3 \rho \quad (4.8)$$

It is important that $\tilde{\omega}$ and \tilde{a} are independent from the density so that the polynomial coefficients are constants. Using these quantities, (4.7) transforms into a polynomial

¹Keep in mind that $\beta\omega(\rho)$ is the DFT free energy functional, and ρ is only a variable. The equilibrium properties are found by minimising the DFT functional. It is thus clear that the functional derivative $\frac{\partial\omega(\rho)}{\partial\rho}$ is always zero for actual (i.e. physical) densities.

of order 5 in η :

$$\begin{aligned}\tilde{\omega} &= \frac{\eta^4 - \eta^3 - \eta^2 - \eta}{(1 - \eta)^3} - \tilde{a}\eta^2, \\ \tilde{\omega}(1 - \eta)^3 &= \eta^4 - \eta^3 - \eta^2 - \eta - \tilde{a}\eta^2(1 - \eta)^3, \\ \tilde{\omega}(1 - 3\eta + 3\eta^2 - \eta^3) &= \eta^4 - \eta^3 - \eta^2 - \eta - \tilde{a}\eta^2(1 - 3\eta + 3\eta^2 - \eta^3),\end{aligned}\tag{4.9}$$

which gives

$$\boxed{\tilde{a}\eta^5 + (1 - 3\tilde{a})\eta^4 + (-1 + \tilde{\omega} + 3\tilde{a})\eta^3 + (-1 - 3\tilde{\omega} - \tilde{a})\eta^2 + (-1 + 3\tilde{\omega})\eta - \tilde{\omega} = 0.}\tag{4.10}$$

4.3 The fluid-solid coexistence

To find the coexistence point between the solid and any fluid phase, we have to perform several computations for different thermodynamic conditions (kT, μ) and compare the free energy per unit volume $\beta\omega$ for each phase. As explained in section 3.4, free energy minimisation in fluid phases can lead to several minima. When multiple minima exist, we select the one corresponding to the type of coexistence curve that we want to compute. This happens when either the vapour or liquid phase is stable and the other is metastable. So, if we want to compute the vapour-solid coexistence, we select the vapour solution whether or not it is the most stable phase relative to the liquid.

Our procedure is to start with an arbitrary value of the chemical potential. For this value, we minimise the solid density profile as explained in sections 3.7 and 3.6. This gives us the solid free energy (per unit volume) $\beta\omega_S$ and other physical quantities². We also minimise the fluid phase free energy function to get the fluid density ρ_F and free energy (per unit volume) $\beta\omega_F$. Then, we can do the same for neighbour values of the chemical potential and move in the direction where the free energy difference $\beta\omega_S - \beta\omega_F$ goes to zero, with a fixed step between one value of the chemical potential and the other. This is repeated until we cross the zero of $\beta\omega_S - \beta\omega_F$.

Once we have covered a range of chemical potentials that contains the coexistence point, we interpolate the results. The interpolation method that we use is a cubic spline from the GSL library [29]. We then solve the root-finding problem $\beta\omega_S - \beta\omega_F = 0$ using the bisection method. The bisection algorithm stops when it reaches a relative precision of 10^{-8} .

²We keep track of the average solid density ρ_S , the lattice constant in number of grid points N_{grid} , the vacancy concentration c_{vac} and the gaussian width parameter α .

4.4 Extraction from simulation data

The coexistence curves that we generate using our DFT model must be compared with simulation results in order to check the ability of the DFT functional to reproduce the qualitative features of the potentials. The literature contains several works that report simulation data for the Lennard-Jones potential. The article of Wang et al. [17] introducing the WHDF potential also includes the necessary data to reproduce the coexistence curves.

In the article of Wang et al., the simulation data is reported under the form of fits of the excess Helmholtz free energy per unit volume $\beta\rho a_{ex}$. For the liquid phase, the free energy is developed as

$$\beta\rho a_{ex}^L = \sum_n \sum_m a_{nm}^L \rho^n \beta^m. \quad (4.11)$$

and the same expansion is used for the vapour, with other coefficients. For the solid phase, an additional term takes into account the low temperature harmonic behaviour:

$$\beta\rho a_{ex}^S = \frac{3}{2}\rho \ln \beta + \sum_n \sum_m a_{nm}^S \rho^n \beta^m. \quad (4.12)$$

We can use the following thermodynamic relations to extract the excess pressure and chemical potential:

$$\begin{aligned} \beta p_{ex} &= -\beta\rho a_{ex} + \rho \frac{\partial}{\partial \rho} (\beta\rho a_{ex})_T, \\ \beta\mu_{ex} &= \frac{\partial}{\partial \rho} (\beta\rho a_{ex})_T. \end{aligned} \quad (4.13)$$

Introducing the decomposition scheme of $\beta\rho a_{ex}$ we get the excess pressures and chemical potential in terms of the fit coefficients:

$$\begin{aligned} \beta p_{ex}^{L,S} &= \sum_n \sum_m (n-1) a_{nm}^{L,S} \rho^n \beta^m \\ \beta\mu_{ex}^L &= \sum_n \sum_m n a_{nm}^L \rho^{n-1} \beta^m \\ \beta\mu_{ex}^S &= \frac{3}{2} \ln \beta + \sum_n \sum_m n a_{nm}^S \rho^{n-1} \beta^m \end{aligned} \quad (4.14)$$

Our strategy to find the coexistence curves is to start with an initial guess of the coexistence density for phase 1, ρ_1 , compute the associated densities at the same pressure and chemical potential for phase 2, and then compare both densities

predicted for phase 2. At coexistence, the densities for phase 2 at same pressure and same chemical potential must be equal. This is because in the canonical ensemble in which simulations are performed the coexistence conditions are the equilibration of both pressures and chemical potentials. The steps for the initial guess are thus repeated for neighbour densities in phase 1, $\rho_1 \pm \Delta\rho$, and we move by steps of $\Delta\rho$ in the direction where the two predicted densities for phase 2 get closer. Once we cross the equality for the predicted densities, we turn back with a smaller step. We repeat this process until we are sufficiently close to the coexistence point.

For the Lennard-Jones potential, we simply extract the coexistence curves from an image of the phase diagram using a web application [31]. The phase diagram was computed by Schultz et al. [30] using hybrid Monte Carlo and Molecular Dynamics simulations. It turns out the extracted data is sufficiently for the comparisons we do.

The comparison with simulation results are given in the next chapter, along with the DFT calculations.

Chapter 5

Phase diagrams

5.1 Introduction

In chapter 3, we presented the DFT model, its implementation and the techniques we used to minimise the DFT functional. In chapter 4, we explained how this DFT framework can be used to compute phase coexistence curves. In this chapter, we discuss the phase diagrams that we get by compiling the phase coexistence curves that we computed.

The phase diagrams are presented in a graph using the density ρ as abscissa and the temperature kT as ordinate. An example is presented on Fig. 5.1 for explanatory purposes. Coexistence curves delimits the stability region of a given phase. For example, the liquid phase is stable in the region indicated with the label L on the figure. If the density increases, we get closer to the liquid-solid coexistence line (in green) and the liquid progressively loses stability in favour of the solid phase. The solid first becomes metastable, then equally stable when standing on the coexistence line. If we cross the coexistence line, the solid becomes the most stable phase and the liquid becomes metastable, then eventually loses the metastability. Note that the transition is not continuous: during the transition from a liquid to a solid phase, the system contains two phases separated by an interface. In each phase, the density is given by the coexistence curve (indicated by a dot on the figure). The average density in the system is somewhere between the coexistence liquid and solid densities, going from one to the other as the transition progresses. However, no actual phase exists in the region between the coexistence curves. This region is unstable (or metastable) for both phases in coexistence.

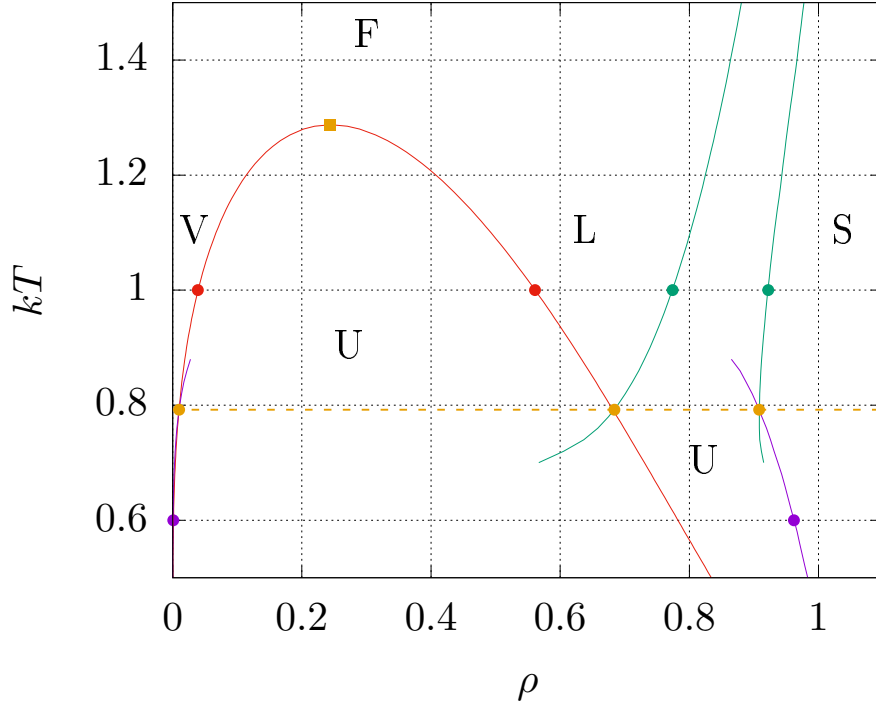


Figure 5.1 – Example of phase diagram in the (ρ, kT) plane. Coexistence curves are shown in different color according to their type. Dots indicate example of coexisting densities at fixed temperature. Coexisting phases are always represented in the same color. Red is associated with the vapour-liquid coexistence, purple with vapour-solid and green with liquid-solid. The yellow square indicates the critical point and the dashed yellow line marks the triple point temperature. The labels V,L,S show the location of the vapour, liquid and solid phases. Label F stands for "fluid" and shows the location of the supercritical fluid. Label U indicates regions of the phase diagram that are unstable. This diagram is an illustration, built using the data we collected from our DFT computations. It does not constitute a report of our results.

5.2 Simple fluids

Phase diagrams for simple fluids are reported on Fig. 5.2. The first shows the coexistence curves obtained for the Lennard-Jones potential and the second shows results for the WHDF potential with the cut-off parameter $r_c = 2$. Next to our DFT computations, the figures also display results from simulation. Qualitatively, the DFT model reproduces all important features of the diagram. It has critical and triple points and the coexistence curves are reproduced with reasonable shapes and positions.

The effect of the cut-off on the Lennard-Jones coexistence results is visible on Fig. 5.3. Phase diagrams are computed for several values of the cut-off ($r_c = 3$, $r_c = 4$ and $r_c = 10$) and superposed. The most visible change is the position of the vapour-liquid coexistence line, that is shifted to higher temperatures as the cut-off increases.

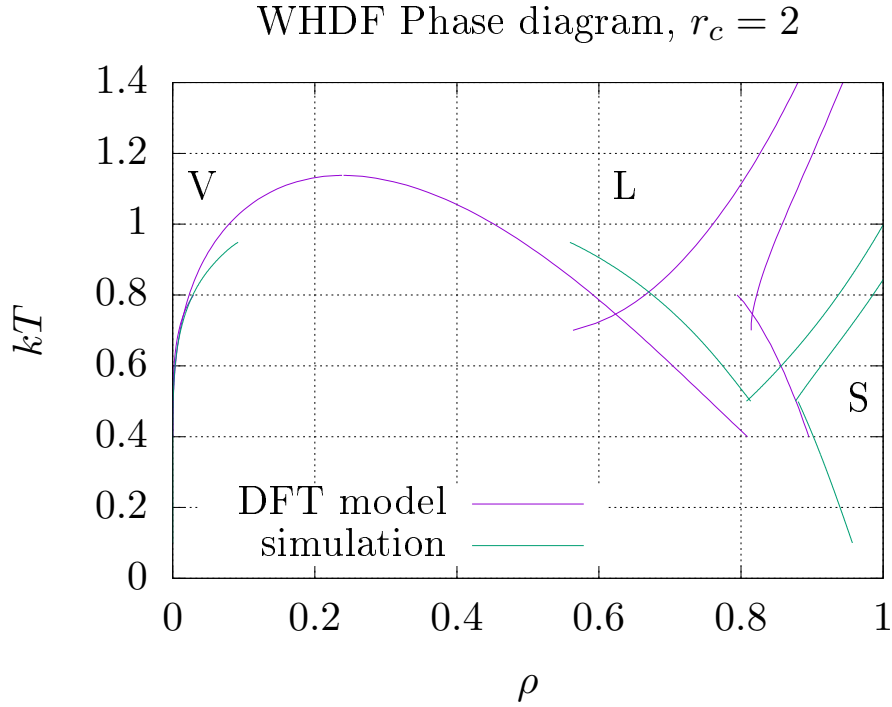
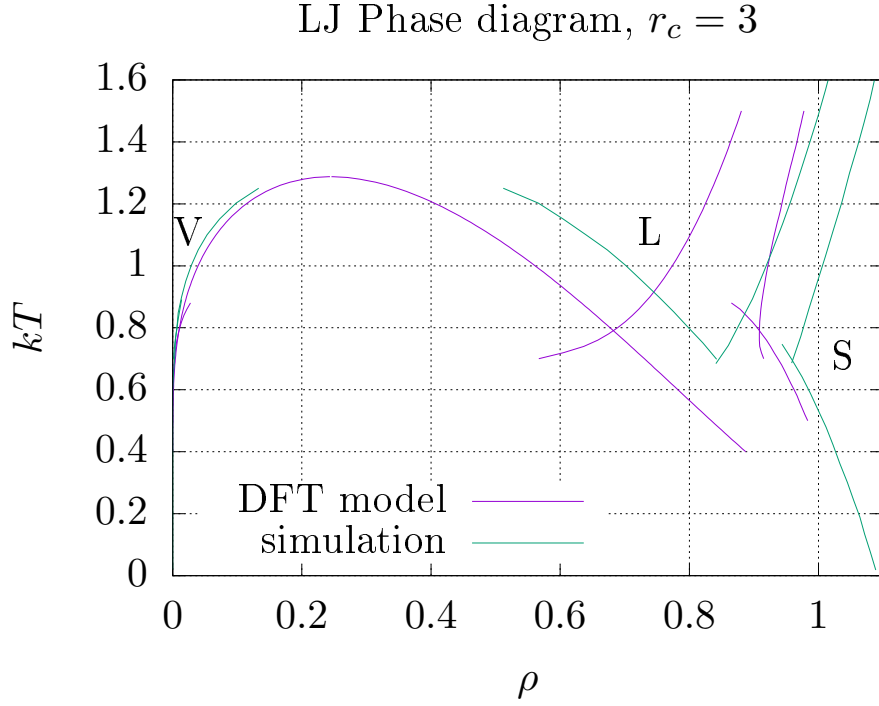


Figure 5.2 – (top) Phase diagram for the Lennard-Jones potential. The purple curves show the coexistence lines from the DFT computations, which use a cut-off $r_c = 3$. The blue curves show coexistence lines obtained by simulation [30]. The simulations use a variable cut-off, closer to $r_c = 10$. The labels V,L and S indicate the location of the vapour, liquid and solid phases. (bottom) The same for the WHDF potential, with a cut-off $r_c = 2$ for both DFT and simulation [17].

Effect of the cut-off (LJ)

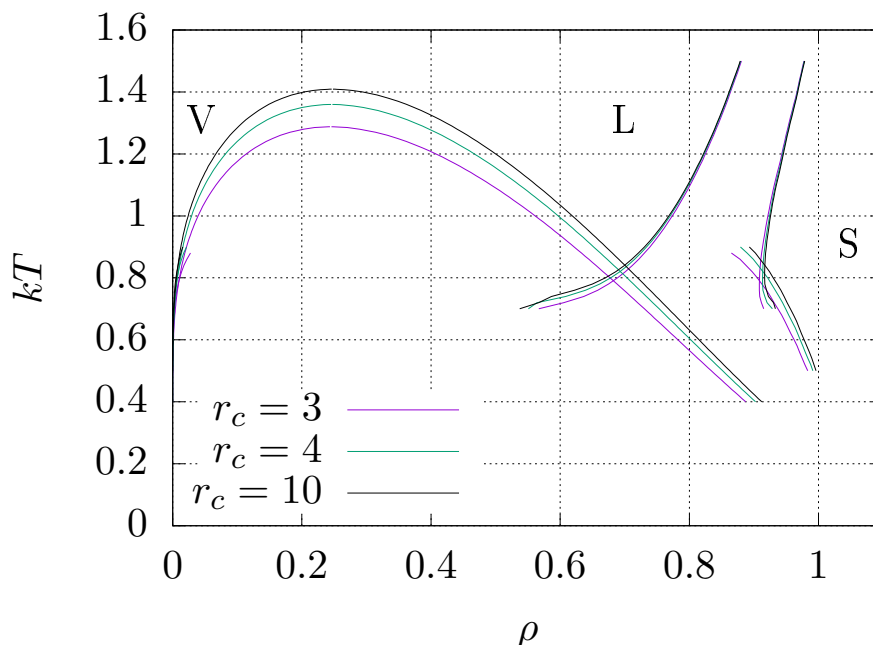


Figure 5.3 – Phase diagrams for the Lennard-Jones potential, using different values of the cut-off r_c .

The critical point is thus moved to higher temperatures. By the same effect, the triple point is also shifted but the shift is not as large. This effect of the cut-off on the vapour-liquid coexistence curve was expected, as it is already well known from simulation results. It is however reassuring that the DFT reproduces this behaviour. An other point to be made is that changing cut-off only shifts the coexistence curves along the temperature axis, there is little difference in densities. The cut-off doesn't seem to play any role in the difference between DFT and simulation results.

A noticeable thing is that the coexistence curves from DFT can extend into an unstable region after crossing another coexistence line. This happens at a triple point where an equilibrium between two phases is disturbed by the presence of a third. The stability switches from one phase to the other and the phase that was initially stable becomes metastable. The ability to resolve metastable states is a remarkable feature of the DFT framework. In simulation, these states are difficult to observe. The existence of metastable states and their importance for the study of nucleation has been stated quite recently [6].

5.3 Colloids

The phase diagram for the WHDF potential with cut-off $r_c = 1.2$ (colloid-like interaction) is reported on Fig. 5.2. As we did with the simple fluid diagrams, the

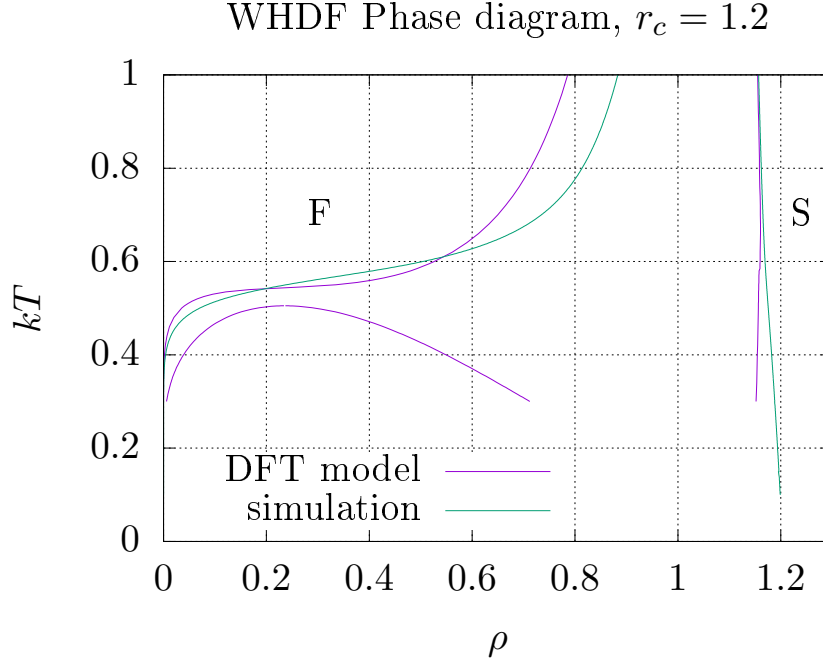


Figure 5.4 – Phase diagram for the WHDF potential, with a cut-off $r_c = 1.2$ to model colloids. Both DFT and simulation use the same cut-off. Labels F and S indicate the location of fluid and solid phases. The simulation data is from [17].

DFT computations are displayed next to the simulation results. The comparison shows that for this type of potential too the DFT is able to reproduce the expected behaviour, at least qualitatively.

In the case of colloids, the most important feature that needed to be recovered is the fact that the vapour-liquid coexistence curve is located below the fluid-solid one, on the temperature axis. This is a particular property of colloid systems that had to be present in the DFT model, in order to use it for future work on protein crystallisation. It comes from the fact that this coexistence curve shows the location (and presence) of metastable states in the unstable region between the fluid and solid at low temperatures, as we explained in a previous paragraph. These metastable states are likely to appear on the reaction path during the transition from the fluid to solid phase. In protein research, this kind of phenomenon has attracted attention under the term of metastable liquid-liquid transitions [32].

Last, we can underline the fact that for the WHDF potential, DFT is able to reproduce to change of nature of the interaction, from simple fluid to colloid, that can be done by changing the cut-off. This is a primary feature of this potential that the DFT recovers using the same values for the cut-off parameter that have been used in simulation [17].

Chapter 6

Critical and triple points

6.1 Critical point

The critical point is the point in the phase diagram where the coexisting vapour and liquid densities merge. This happens at a temperature above which these two phases become indistinguishable, forming what is called a supercritical fluid. Figure 6.1 shows what happens to the free energy profile near the critical point. At low temperatures, the free energy profile presents two minima, corresponding to the vapour and liquid phase, respectively at low and high densities. On the coexistence line, these two minima are associated to the same free energy. When the temperature increases these two wells get closer from each other. They merge at the critical temperature, above which only one minimum remains.

The typical behaviour of the free energy functional near the critical point can be described with a double well model ¹, where the free energy is approximated with only quadratic and quartic terms:

$$\beta\omega(\rho) - \beta\omega_c = \frac{1}{2}a(\rho - \rho_c)^2 + \frac{1}{4}b(\rho - \rho_c)^4, \quad (6.1)$$

where $b > 0$ and the subscript c indicates a value at the critical point. Under the critical temperature, the factor a of the quadratic term must be negative, to allow the presence of the two wells that we observe. Above, it must be positive as there is only one well left. It must therefore vanish at the critical temperature.

This picture helps us to formulate conditions on the free energy derivatives. We already know that the first derivative of the free energy is zero from the basics of density functional theory: the equilibrium density is the one that minimises the

¹We must keep in mind that the density in this expression is the input variable of the free energy functional, not the physical density. The physical density is the density that minimises the free energy functional.

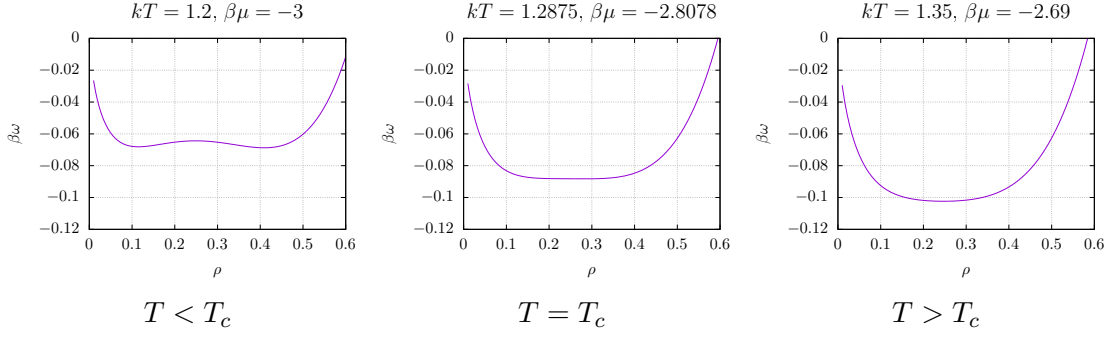


Figure 6.1 – Behaviour of the free energy profile near the critical point. These figures have been generated using the Lennard-Jones potential with a cut-off $r_c = 3$.

free energy functional. We have seen that the second derivative must vanish at the critical temperature to create the transition from two wells to one. Additionally, the double well model requires the third derivative to be zero at the critical point so that no third-order correction $(\rho - \rho_c)^3$ appears. Another justification for the cancellation of the third derivative is that without it, the two wells would be at different heights, indicating that the vapour and liquid phases are not coexisting. This would contradict the fact that the critical point lies on the vapour-liquid coexistence line. We can also notice that the third derivative does not need to vanish elsewhere on the critical temperature isotherm, where the vapour and liquid phases do not coexist.

It is these conditions on the derivatives, along with the fact that the free energy functional is a simple, ordinary function in the case of uniform densities, that will allow us to locate the critical point in this DFT model. In section 3.4, we derived the following expression for the free energy per unit volume:

$$\beta\omega(\rho) = \rho \ln \rho - \rho + \rho \frac{\eta(4 - 3\eta)}{(1 - \eta)^2} + a\rho^2 - \beta\mu\rho. \quad (6.2)$$

We get for its derivatives

$$\beta \frac{\partial \omega(\rho)}{\partial \rho} = \ln \rho + \frac{\eta(3\eta^2 - 9\eta + 8)}{(1 - \eta)^3} + 2a\rho - \beta\mu, \quad (6.3)$$

$$\beta \frac{\partial^2 \omega(\rho)}{\partial \rho^2} = \frac{1}{\rho} + \frac{\eta}{\rho} \frac{8 - 2\eta}{(1 - \eta)^4} + 2a, \quad (6.4)$$

$$\beta \frac{\partial^3 \omega(\rho)}{\partial \rho^3} = \frac{1}{\rho^2} \frac{\eta^5 - 5\eta^4 + 4\eta^3 + 20\eta^2 + 5\eta - 1}{(1 - \eta)^5}. \quad (6.5)$$

Note that many of the unknown parameters in the expression of the free energy

do not appear in the derivatives. By the third derivative, the only unknowns are the packing fraction η and the density ρ . Our strategy to find the value of all these quantities $(\eta, \rho, kT, a, \beta\mu, \beta\omega)$ at the critical point is based on the vanishing conditions that we found for the free energy derivatives. We start from the higher order derivatives, which contain fewer parameters, and then substitute the results in the other equations.

We begin with the third-order derivative. Setting its expression to zero gives an equation for η , as the density appears only as a factor of zero. Solving this equation is a simple polynomial root-finding problem:

$$\boxed{0 = \eta^5 - 5\eta^4 + 4\eta^3 + 20\eta^2 + 5\eta - 1} \quad (6.6)$$

Note that this expression involves no external parameter and the critical value of the packing fraction η is therefore the same for any potential. The coefficients of the polynomial only depend on the DFT model itself. This universal value of the packing fraction is

$$\eta \approx 0.13044. \quad (6.7)$$

From the value of η , it is tempting to try getting the density from the expression of η in a uniform phase,

$$\eta = \frac{\pi}{6} d_{hs}^3 \rho. \quad (6.8)$$

However, the hard-sphere diameter d_{hs} depends on the temperature kT . Hopefully, we can find a closed system of equations by using the vanishing condition of the second free energy derivative. This is possible because the Van der Waals parameter, a , only depends on the temperature:

$$a = \frac{1}{2} \int \beta w(r) d\mathbf{r} \equiv \beta a_0, \quad (6.9)$$

where $w(r)$ is the attractive part of the potential (see section 2.6) and a_0 depends only on the potential and on the details of the discretisation. The closed system for kT and ρ is

$$\begin{cases} 0 = \frac{1}{\rho} + \frac{\eta}{\rho} \frac{8 - 2\eta}{(1 - \eta)^4} + 2\beta a_0, \\ \eta = \frac{\pi}{6} d_{hs}^3 \rho. \end{cases} \quad (6.10)$$

Substituting the value of the density in the first equation leads to

$$\boxed{kT d_{hs}^3 = -\frac{12 a_0}{\pi} \frac{\eta(1 - \eta)^4}{\eta^4 - 4\eta^3 + 4\eta^2 + 4\eta + 1}.} \quad (6.11)$$

That is a closed equation for the temperature that we solve numerically due to the non trivial dependence of d_{hs} on the temperature (2.33). We proceed in an iterative manner, beginning with an arbitrary value of the temperature. We compute the right-hand side and subtract the left-hand side, that does not depend on the temperature. We increase or decrease the temperature in order to reach equilibration, decreasing the steps each time we cross it. We stop when we reach a relative precision of 10^{-8} on the critical temperature.

Once η and the temperature kT are known, it is straightforward to compute the remaining quantities. The parameters d_{hs} and a are computed at the same time as kT and the density is computed from η and d_{hs} using (6.8). At this point, we know all the necessary parameters to compute the chemical potential $\beta\mu$ and the free energy $\beta\omega$. The first can be isolated from the vanishing condition on the first derivative (6.3) and the other is given by (6.2).

Even though we have everything in hand to compute $\beta\mu$ and $\beta\omega$, we try reducing their expressions to as few parameters as we can. It is not very difficult to find analytical expressions in terms of η and ρ . We can start by isolating the Van der Waals parameter, a , in the second derivative (6.4):

$$0 = \beta \frac{\partial^2 \omega}{\partial \rho^2} \iff a = \frac{1}{2\rho} + \frac{\eta}{\rho} \frac{4 - \eta}{(1 - \eta)^4}. \quad (6.12)$$

Then, we can substitute a in the first derivative (6.3) and isolate $\beta\mu$:

$$0 = \beta \frac{\partial \omega}{\partial \rho} \iff \beta\mu = \ln \rho - \frac{\eta^4 - 16\eta^3 + 21\eta^2 - 4\eta + 1}{(1 - \eta)^4}. \quad (6.13)$$

Finally, the same can be done for the free energy, for which we can replace a and $\beta\mu$ in expression (6.2):

$$\beta\omega = \rho \frac{7\eta^3 + 7\eta^2 + 3\eta - 1}{2(1 - \eta)^3}. \quad (6.14)$$

By doing this reduction, we can see if some quantities are independent of the potential, and so have a fixed value in the DFT model. This is true for quantities that can be expressed in terms of η only, as η has itself such property. We find that the excess chemical potential, $\beta\mu_{ex} = \beta\mu - \ln \rho$ and the free energy per particle $\beta\omega/\rho$ are both independent of the potential, in this DFT model. Their values are

$$\beta\mu_{ex} = \frac{\eta^4 - 16\eta^3 + 21\eta^2 - 4\eta + 1}{(1 - \eta)^4} \approx -1.39984 \quad (6.15)$$

$$\text{and } \beta\omega/\rho = \frac{7\eta^3 + 7\eta^2 + 3\eta - 1}{2(1 - \eta)^3} \approx -0.36048. \quad (6.16)$$

property	value
kT	1.2875
ρ	0.2446
$\beta\mu$	-2.8079
$\beta\omega$	-0.0881
d_{hs}	1.0061
a	-5.6530

Table 6.1 – Critical properties of the Lennard-Jones potential with cut-off $r_c = 3$.

property	value
kT	1.3595
ρ	0.2462
$\beta\mu$	-2.8016
$\beta\omega$	-0.0888
d_{hs}	1.0040
a	-5.6175

Table 6.2 – Critical properties of the Lennard-Jones potential with cut-off $r_c = 4$.

The critical properties of the studied potentials are tabulated in tables 6.1, 6.3 and 6.4. We can note that many properties take similar values across all studied potentials. This is because the potentials have a repulsive core at roughly the same distance, in terms of the length parameter σ . The effective hard sphere diameter d_{hs} is thus always close to 1 and the density, which depends only on d_{hs} and η (6.8), is therefore fixed by the value of η at the critical point,

$$\rho = \frac{6\eta}{\pi d_{hs}^3} \approx \frac{6\eta}{\pi} = \frac{6 \times 0.13044}{\pi} \approx 0.249. \quad (6.17)$$

The chemical potential and free energy per unit volume are almost unchanged as well because they depend only on ρ and η (6.13)(6.14). The temperature however is not fixed by these quantities and is free to take very different values. The consequence on phase diagrams is that changes in the potential move the vapour-liquid coexistence curves mainly along the temperature axis, as we can see on the diagrams presented in chapter 5. This also relates to the fact that potentials with shorter range for the attractive interaction have a critical point at lower temperature. We can see this from the formula of the Van der Waals parameter (6.9) that it is proportional to the inverse temperature and to the integral of the attractive part of the potential. It is also relatively constant at the critical point as it can be expressed in terms of the ρ and η only (6.12). The result is that with a shorter range, the integral takes a smaller value which must be compensated by a larger inverse temperature. Thus, we can see why colloid-like interactions, having a short-ranged attraction, can end up with a critical point below the fluid-solid coexistence curve on the temperature axis.

property	value
kT	1.1378
ρ	0.2394
$\beta\mu$	-2.8296
$\beta\omega$	-0.0863
d_{hs}	1.0134
a	-5.7770

Table 6.3 – Critical properties of the WHDF potential with cut-off $r_c = 2$.

property	value
kT	0.5051
ρ	0.2355
$\beta\mu$	-2.8458
$\beta\omega$	-0.0849
d_{hs}	1.0189
a	-5.8713

Table 6.4 – Critical properties of the WHDF potential with cut-off $r_c = 1.2$.

6.2 Triple point

The triple point is defined as the point in the space of thermodynamic parameters, e.g. (kT, μ) , for which the vapour, liquid and solid phases can all coexist. On the temperature-density phase diagram, the triple point is split over three densities, corresponding to each phase. It is better represented as a line indicating the triple temperature, as we have shown on Fig. 5.1. The intersection between this line and a coexistence curve gives the density of the corresponding phase at the triple point.

The triple temperature is also the temperature at which the vapour-solid and the liquid-solid coexistence lines intersect. We use this property to compute the triple point properties, using the data collected during phase coexistence computations. Our method is to fit the solid density in function of the temperature, from both vapour-solid and liquid-solid coexistence data. We then compute the intersection of the two fits which gives the triple point temperature as well as the solid density. Other quantities are computed similarly, by fitting their coexistence value in function of the temperature and then by evaluating these fits at the triple point temperature. Using this procedure, we compute the triple point values of all quantities we recorded during coexistence computations. The triple point properties of the studied potentials are displayed in tables 6.5 and 6.6.

property	value
kT	0.7918
ρ_V	9.808×10^{-3}
ρ_L	0.6841
ρ_S	0.9082
$\beta\mu$	-4.760
$\beta\omega$	-9.146×10^{-3}

Table 6.5 – Triple point properties of the LJ potential with cut-off $r_c = 3$.

property	value
kT	0.7464
ρ_V	1.545×10^{-2}
ρ_L	0.6227
ρ_S	0.8160
$\beta\mu$	-4.369
$\beta\omega$	-1.392×10^{-2}

Table 6.6 – Triple point properties of the WHDF potential with cut-off $r_c = 2$.

Chapter 7

Vacancy concentrations

7.1 Vacancies along coexistence curves

The process of minimising the DFT functional outputs the concentration of vacancies in the equilibrium solid phase, i.e. vacant sites in the lattice structure. We kept track of it while computing phase diagrams, in order to interpolate its value on the coexistence curves. The vacancy concentration is a very sensitive quantity and usually shows an exponential dependence on temperature and density. This makes it a good diagnostic quantity to evaluate the quality of a DFT model.

Figure 7.1 displays the vacancy concentrations that we get on the vapour-solid and liquid-solid coexistence curves in the case of simple fluid potentials. At vapour-solid coexistence, the concentration of vacancies increases exponentially with the temperature. On the liquid-solid coexistence line, it is expected that the vacancy concentration does not change significantly with the temperature (see next section). The overall behaviour of the vacancy concentration is quite good. We can however spot two anomalies on this graph.

The first anomaly is located at low temperatures and is the most obvious. The vacancy concentration at the vapour-solid coexistence suddenly increases as the temperature drops below a certain threshold. After a bit of investigation, we realised that this anomaly comes from the way we perform spherical integrations during the evaluation of the free energy functional using pre-compiled numeric weights (see section 3.2). At low temperatures, the computation is incorrect as the actual minimum is in the region where the free energy functional diverges¹. With the pre-compiled weights, the functional minimum is shifted close to the border of the region where the functional diverges. This results in an overestimation of the vacancy concentration at the minimum.

¹cf. discussion in appendix C, and figure C.1 in particular

Vacancies along coexistence curves

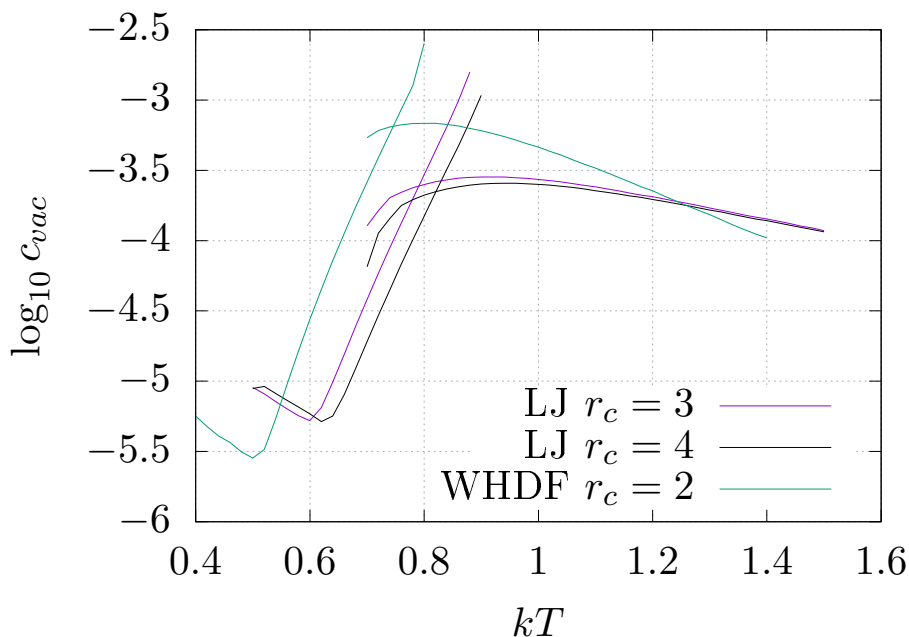


Figure 7.1 – Vacancy concentration along vapour-solid and liquid-solid coexistence curves for potentials modelling simple fluids.

The second anomaly is that at high temperature, is that the vacancy concentration decreases at high temperatures. We will discuss this behaviour in the next section.

For the colloid-like potential, WHDF $r_c = 1.2$, the computation of vacancies is more complicated. Figure 7.2 shows the concentration of vacancies that we computed along the fluid-solid coexistence curve. Our default procedure is to use quadratic interpolations, but the results that we get for vacancies in this potential present a large variability. The interpolated values are therefore very sensitive to the interpolation method. Figure 7.2 also shows what we obtain by using cubic spline interpolations instead. This variability seems to be caused by the fact that the grid spacing is too large. We discuss this problem in more depth in appendix C, where we show how the numerical limitations we faced affect calculations of the free energy profile. As a result of this imprecision, the data for the vacancy concentration at low temperatures is incorrect and can only be considered as preliminary. In contrast, the results for temperatures above $kT \approx 0.85$ are not affected by this problem and we can see that we obtain similar values as those observed in simple fluids. We therefore conclude that despite the technical difficulties, we still get a concentration of vacancies at an order of magnitude consistent with our expectations.

Vacancies along coexistence curves WHDF $r_c = 1.2$

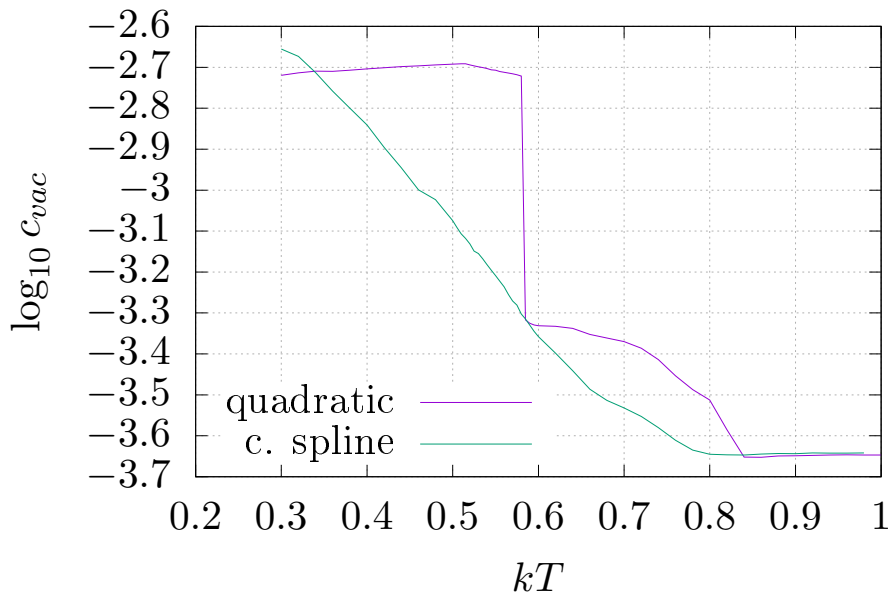


Figure 7.2 – Vacancy concentration along the fluid-solid coexistence curve for the WHDF potential ($r_c = 1.2$) modelling colloids, using two interpolation methods. The data below $kT \approx 0.85$ is subject to numerical errors and must be interpreted with caution.

7.2 Comparison with simulations

Simulation results for the Lennard-Jones potential were found in an article from Purohit et al. [33]. This group performed simulations of the Lennard-Jones FCC solid and provided detailed results on vacancy concentrations.

A major difficulty in comparing vacancy concentrations is that phase diagrams from DFT and simulations are quite different quantitatively (see Fig. 5.2) and the vacancy concentration is very sensitive to the temperature and density. Therefore, it doesn't make much sense to compare vacancy concentrations at the same temperature and density as they actually correspond to two different points on the phase diagram. However, the vacancy concentration doesn't change very much on the liquid-solid coexistence curve. This is true for the simulation data but it is also the case for our DFT calculations. It thus seems to make sense to compare vacancy concentration near the liquid-solid coexistence.

Their results for vacancy concentrations are reported on a graph from which we extract numerical data using a web application [31]. They expressed the simulation results in terms of combinations of temperature and density that are more convenient to use in the soft sphere limit (high temperatures and densities). We select only the

dots in their graph near liquid-solid coexistence. The extracted data, converted to temperature and density variables, is shown on Fig. 7.3 next to our DFT results. We associate an uncertainty to the data based on the uncertainty reported in the graph of Purohit et al., which indicated that error bars on the graph were smaller or about the size of the dots used to mark the data points. In our own figure (7.3), we thus reported an error the size of their dots.

The simulations are performed with a variable cut-off, given by $r_c = 4\tilde{v}^{-1/3}$. This value is $r_c = 4.0 \pm 0.1$ for our range of temperature ($0.9 < \tilde{v} < 1.1$). For comparison, we thus use our DFT results with $r_c = 4$. However, we previously noted that the vacancy concentrations at liquid-solid coexistence doesn't change much with the cut-off (see Fig. 7.1).

Figure 7.3 shows that the concentrations of vacancies computed using our DFT model have the right order of magnitude, at least for low temperatures ($kT < 2$). At high temperature however, the simulations show that the vacancy concentration remains approximately constant. In contrast, the concentrations predicted by DFT decrease in an exponential manner with the temperature.

Despite looking quite bad, the high temperature deviations are not that surprising. This can be expected because of the exponential dependence on temperature and density. As the vacancy concentration is so sensitive, small errors in determining the location of the coexistence line will cause exponential deviations in the vacancy concentration. Furthermore, small errors can come from many places as DFT models are approximations. Imprecisions are made in the functional expression itself, in the parametrisation we choose for the solid density and even in the way we minimise it and find coexistence curves. The point is that the sensitivity of the vacancy concentration makes it a good diagnostic quantity for DFT models. Obtaining a concentration of vacancies that is the right order of magnitude is already a good indication of the quality of the DFT model.

Additionally, Fig. 7.4 shows the vacancy concentration computed in other DFT studies found in the literature. We reported results from Mc.Rae et al. [34] and Singh et al. [35]. These studies date from 1990 and 2007, respectively. Their models use older functionals and we can therefore expect that our computations give results closer to the simulations. This is indeed what the comparison shows, as we see on Fig. 7.4. We can still underline the fact that our results do not produce worse result and that indeed progress is made as the DFT models evolve with time.

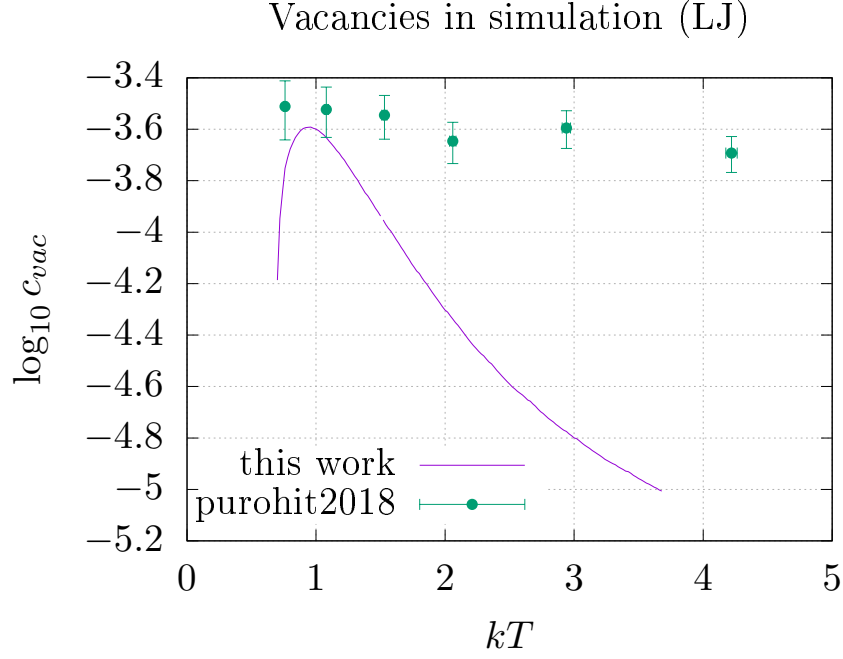


Figure 7.3 – Comparison of vacancy concentrations data from simulations (green dots) [33] and from our DFT computations (purple curve).

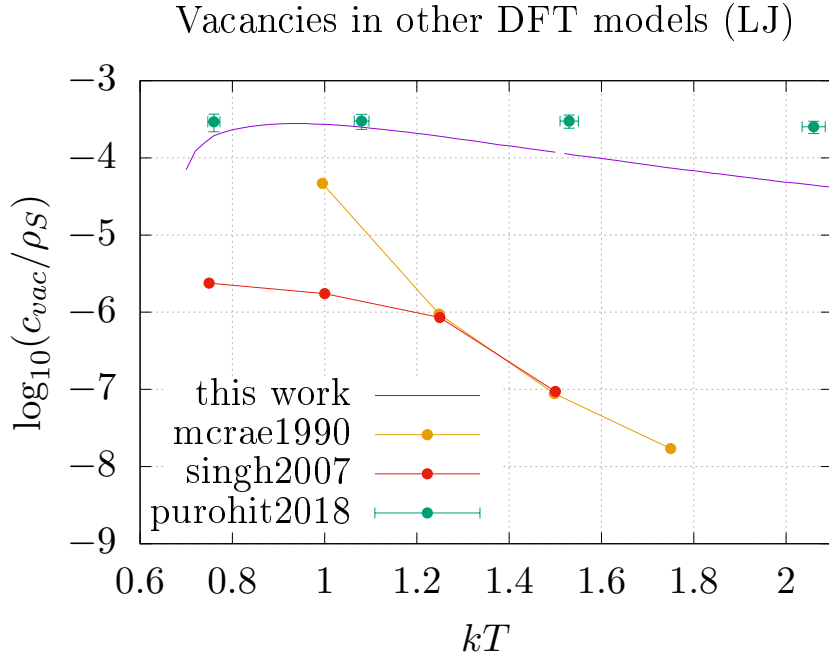


Figure 7.4 – Comparison of vacancy concentrations from different DFT calculations. This graphs show our results (purple curve) next to calculations from [34] and [35]. The green curve shows simulation results from [33]. The data was extracted from figures in these articles using a web application [31].

Chapter 8

FCC-HCP polymorphism

8.1 Implementation

In a crystalline solid, the density field peaks around points of a lattice, forming a periodic structure. Until now, we discussed DFT computations in which we model the solid density as gaussian curves centred around the sites of a FCC lattice. This is indeed not the only possible lattice for a solid. The FCC lattice is a very common structure observed in nature and is one of simplest to implement on a computational grid. However, nothing certifies that this configuration is the most stable in our DFT model. In nature, it is common to find the same compound in more than one possible lattice structure. This phenomenon is called polymorphism. A well known example is the case of calcium carbonate, which exhibits two naturally-occurring polymorph: Calcite (hexagonal lattice) and Aragonite (orthorhombic lattice). In simulations, the group of Wang et al. [17] showed that in the case of their WHDF potential, the HCP lattice (hexagonal closed-packed) is in some cases slightly more stable than FCC. In this chapter, we explain how we implement DFT computations for the HCP lattice and investigate the relative stability of the FCC and HCP configurations.

The HCP lattice is a particular case of the hexagonal lattices family that maximises the packing fraction of hard spheres. It is actually one of the two lattices that maximise this quantity, the other one being the FCC lattice ¹. These two structures are very similar and only differ by their second neighbour (see Fig. 8.1). The major difference is that the HCP lattice does not have a cubic symmetry and, to our knowledge, cannot be implemented on a cubic computational grid with periodic

¹See https://en.wikipedia.org/wiki/Close-packing_of_equal_spheres for more details on the packing of hard sphere and the similitude between the FCC and HCP lattices.

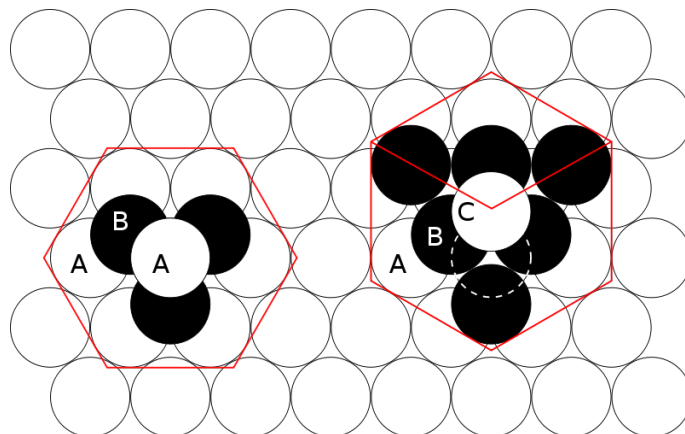


Figure 8.1 – Differences between the FCC and HCP structures. When stacking equal spheres, two possibilities arise for the placement of the third layer. (right) The HCP structure results from placing the third layer exactly above the first, making another layer of type A. (left) The FCC structure results from placing the third layer in the other holes, therefore creating a new type of layer, C, not aligned with A. Figure taken from Wikipedia, https://en.wikipedia.org/wiki/Close-packing_of_equal_spheres the 11th of June, 2020.

boundary conditions². The problem is that the lattice constants, i.e. the length of the edges of the cell, have irrational ratios between one another. That means that we could for example use a rectangular cell for the HCP lattice (see Fig. 8.2), but it would have irrational side lengths.

The rectangular cell is the shape we used as it is easy to implement with periodic boundary conditions. However, as we explained in section 3.5, we choose to work with a fixed grid spacing, identical in all dimensions. For that reason, we can only have cells with side lengths that are multiples of the grid spacing. We thus cannot compute the HCP properties directly. Instead, we perform computations for hexagonal lattices near close-packing, and interpolate the values for the ideal close-packed lattice (i.e. HCP). More precisely, we first compute the rectangle sides that are the closest to the ideal close-packing proportions. This is our reference cell. Then, we generate other rectangular cells by adding $-1, 0$ or 1 times the grid spacing to the side length of the reference cell, for each of the three axis x, y, z . This generates a total of $3 \times 3 = 9$ computational cells. These cells are regular hexagonal lattices near the ideal close-packing fraction. To compute the properties of the HCP lattice, we start by performing DFT computations for each one of these 9 cells. We then interpolate the values for the ideal close-packed lattice (i.e. HCP). The interpolations are done with parabolas, along each axis successively. This is why we use 9 regular lattices: we need three points for each interpolation in x, y, z .

² Interestingly, when trying to figure out how to implement the HCP lattice, we encountered a published article claiming to have a way of implementing the HCP structure on a cubic grid with periodic boundary conditions. We tried their implementation but we observed that the result is not a HCP lattice. The first neighbours of a point generated by their method do not arrange in a tetrahedron, like we expect in the HCP lattice. The reference is: *The Journal of Chem. Phys.* 123, 056101 (2005) <https://doi.org/10.1063/1.1997138>.

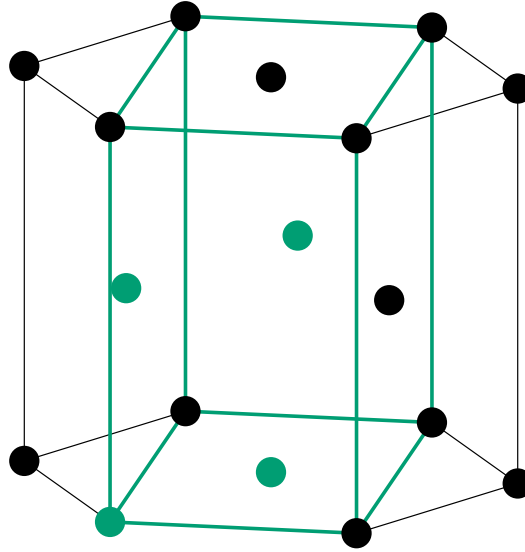


Figure 8.2 – The HCP structure. The blue lines highlight the borders of the rectangular cell used for computations. The blue dots are the lattice sites which constitute the basis of the rectangular cell.

8.2 Results

Once we have implemented a way to perform the HCP lattice computations, we use the same techniques than presented in chapters 3 and 4 to minimise the DFT functional and compute coexistence curves. However, a major difference with the FCC calculations is that we have to perform 9 regular hexagonal lattice computations for each ideal close-packed (HCP) computation. This results in much bigger computation times. A consequence is that while we did many computations for the FCC phase and connected them to present smooth coexistence curves, we could only do a few computations for the HCP phase, which are reported as isolated dots on the phase diagrams.

We computed phase diagrams for the WHDF potential, both in the simple fluid case (cut-off $r_c = 2$) and in the colloid case (cut-off $r_c = 1.2$). They are displayed on Fig. 8.3. We did not expect any major difference between the two cases, because of the FCC and HCP structures only differ at the second neighbour (see Fig. 8.1). The diagrams show that the difference is even barely visible.

To tell which configuration is the most stable, we have to take a closer look and compare the free energies of both phases in the same thermodynamic conditions, i.e. at the same temperature and chemical potential. This is what we report on Fig. 8.4, using values of the chemical potential close to the corresponding fluid-solid coexistence.

In the case of the WHDF $r_c = 2$ potential (simple fluids), we obtain free energies slightly lower for the HCP phase. That means the HCP configuration is the most stable in our DFT model, which is consistent with the results of Wang et al. [17]. We must however underline the fact that the free energy differences are very small and may therefore be influenced by precision errors.

In the case of the WHDF $r_c = 1.2$ potential (colloids), our results present a strange behaviour: the free energy difference seems to lower in a linear fashion as the temperature decreases, but suddenly takes a much higher value. We believe that these results suffer greatly from the precision error that we encountered in chapter 7 for vacancies in colloids. This is likely due to limitations by the grid spacing being too large, that prevent accurate computations for highly localised densities. This problem is discussed in more detail in appendix C. For now, the FCC-HCP stability computations for the colloid case can only be considered as preliminary results. To tell which configuration is the most stable, we would have to try using a finer grid, at the cost of even higher computation times.

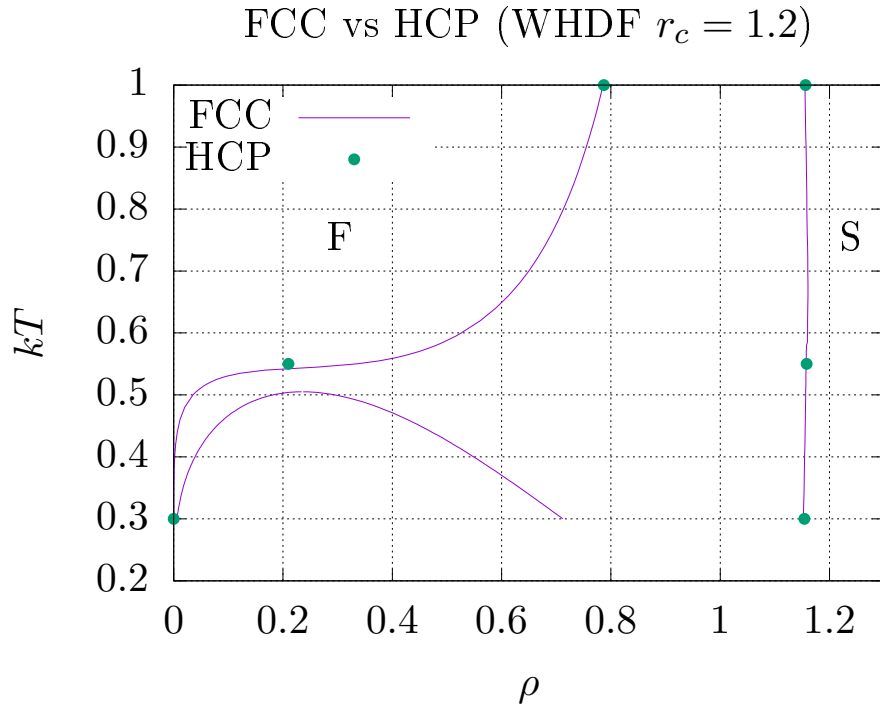
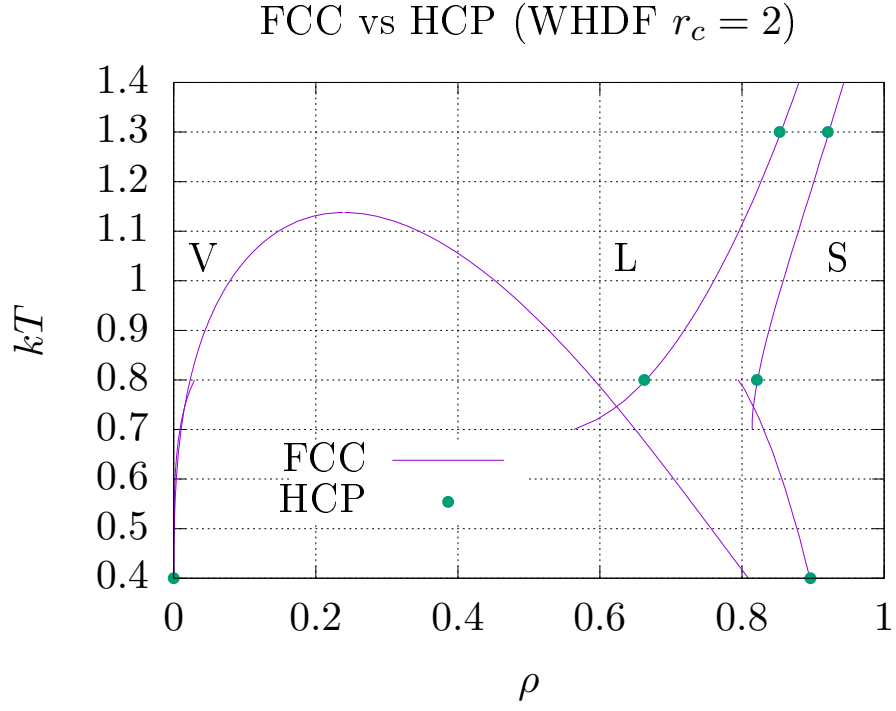


Figure 8.3 – Comparison of phase diagrams with FCC and HCP solid phases. The dots indicates computations with the HCP solid configuration. (top) WHDF potential with a cut-off $r_c = 2$, modelling simple fluids. (bottom) WHDF potential, with a cut-off $r_c = 1.2$, modelling colloids.

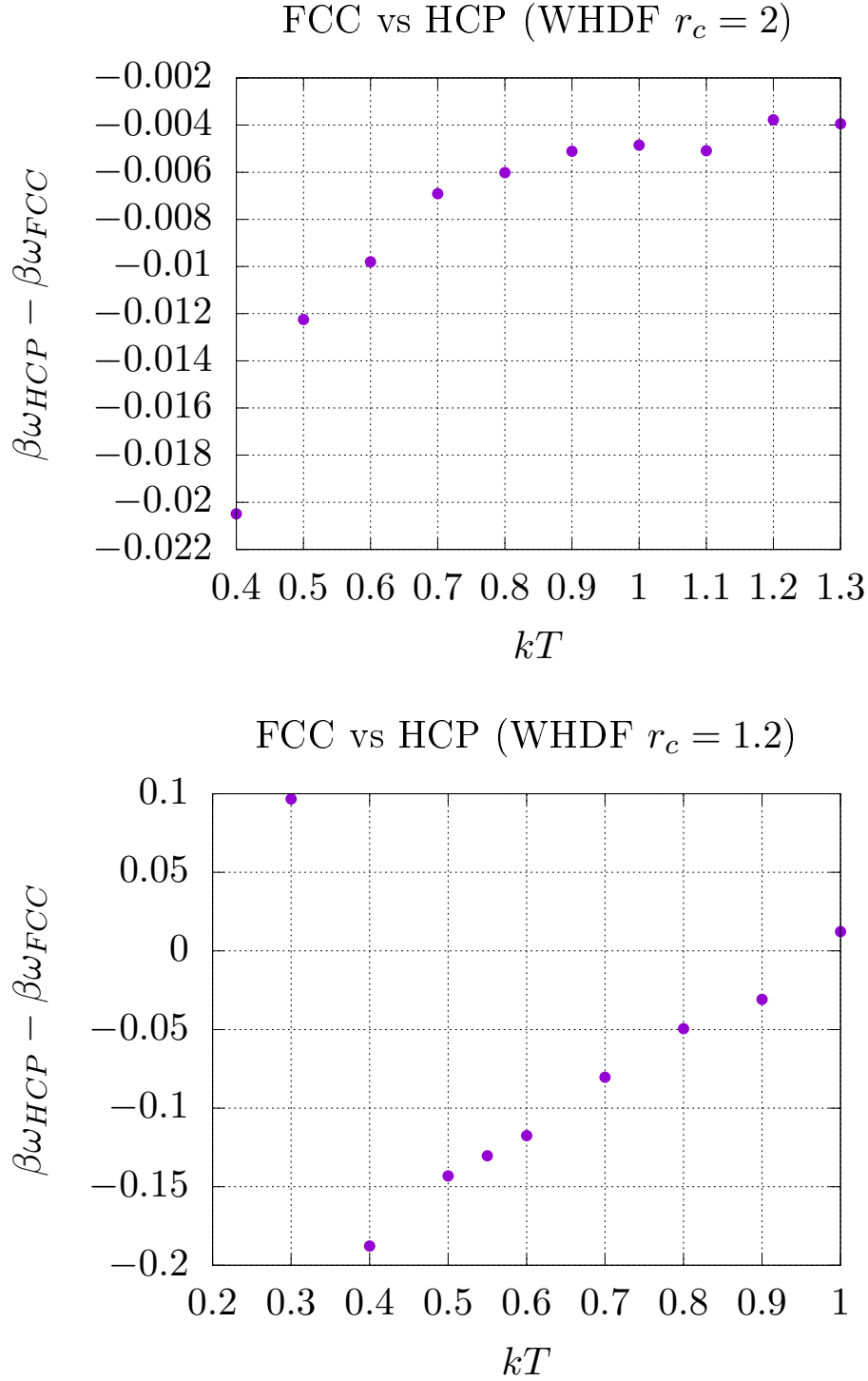


Figure 8.4 – Comparison of the free energies between the FCC and HCP solid phases. For each temperature, the computations of both FCC and HCP phases are performed at the same chemical potential, close to the corresponding fluid-solid coexistence. (top) WHDF potential with a cut-off $r_c = 2$, modelling simple fluids. (bottom) WHDF potential, with a cut-off $r_c = 1.2$, modelling colloids. The bottom graph is subject to precision errors and must be interpreted carefully.

Chapter 9

Conclusions and perspectives

In this master's thesis we made a first step towards applying mesoscopic nucleation theory to the crystallisation of proteins. Our main objective was to compute the phase diagram for a potential modelling colloid-like interactions. We wanted to see if the DFT model presented in the text (mRSLT + mean field interaction) could be used to model the energetics of protein crystallisation.

To achieve this goal, we built on previous work to extend the methods for a broader range of potentials and validated the implementation using previous calculations for the Lennard-Jones potential. At the technical level, this involved a significant amount of numerical analysis. The complications mainly came from the stiffness of the functional, which varies by 10 or more orders of magnitudes over molecular length scales, and the delicate multidimensional minimisation of functions close to singularities.

Once we implemented these techniques, we computed phase diagrams for the WHDF potential, which can model colloid-like interactions as those between proteins. Our DFT model proved adequate to reproduce its phase diagrams, given the usual expectations. We have shown that it reproduces the correct physics qualitatively, in terms of the structure of the phase diagrams, and semi-quantitatively in terms of thermodynamic parameters such as the triple point and vacancy concentrations. Therefore, we have demonstrated that the recently-introduced and numerically stable DFT models, necessary to describe nucleation, can indeed serve as the basis for studying crystallisation in protein-like systems, thus marking an important step towards our ultimate goal.

In addition to the phase diagram, we took a closer look on the vacancy concentrations predicted by our DFT model. By comparison with simulation results, we have shown that our model gives reasonable results for the vacancy concentrations. As this quantity is very sensitive, this observation increase our confidence in the DFT model. We also studied the relative stability of the FCC and HCP configurations for the solid phase and got results similar to those from simulations.

Although the computations were precise enough to compute the phase diagrams, more sensitive quantities like the concentration of vacancies and the FCC-HCP free energy difference were sometimes affected by the grid spacing that we use. This was the case of the colloid-like potential (WHDF $r_c = 1.2$), for which a few computations were inconclusive. In this case, a finer grid seems necessary for more accurate computations.

A natural extension of this work is to go beyond the gaussian parametrisation for the solid. The current state of the art is to perform unconstrained minimisations, where each point of the discretised density field is minimised independently. This allows the description of more general density profiles than just the fluid and the crystalline solid. It is actually an essential tool to model the energetic aspect of nucleation, that has been used in the development of MeNT [13, 11]. We did not include these methods in this work because of practical limitations, but they were developed independently by Lutsko. The results of unconstrained minimisations and the comparison with the data presented in this work will be the subject of future work. At this point in time, the comparison with gaussian calculations already shows good quantitative agreement, even for vacancy concentrations.

Another possible addition to this work is to compute surface tension. This quantity is used in the classical picture of nucleation as a parameter of the capillary model. Knowing surface tension is important to compare the predictions of MeNT with those from the classical theory.

Last, we can note that there is always room to improve the DFT model. Although this is a minor concern to us, the DFT and simulation results could be brought into better quantitative agreement. This may be possible by introducing more complex DFT functionals than those which have commonly been used until now.

Appendix A

Notations and units

A.1 Units

If unspecified, physical quantities are expressed in the correct combination of the potential parameters (ε, σ) , we call them "potential units". This convention is implied in the entire document and was adopted for better readability. A list of the most commonly encountered quantities and their associated potential unit is available in table A.1.

A special note can be made concerning quantities related to energy. Instead of using the potential parameter ε , energy-related quantities are often expressed in "thermal units". They are written with a factor β that indicates that the quantity has been divided by kT . The reported value is thus a multiple of the thermal energy kT , which is more meaningful physically as it relates to the scale of thermal fluctuations. For example, the free energy per unit volume ω is frequently referred to by $\beta\omega$.

We can also note that logarithm arguments like the density in $\ln(\rho\sigma^3)$ are often written alone, not using the correct adimensional combination explicitly. The reference scale, here the length σ , is implied as it is in the unit convention.

A.2 List of symbols

See table A.1 for a list of symbols used for quantities that are often associated with numerical values. Next to the symbol is reported the correct unit combination in potential units in which the numerical value must be interpreted. Table A.2 displays symbols for quantities that appear outside of numerical context, for which giving the unit combination is not relevant.

quantity	symbol	unit
temperature (converted to thermal energy)	kT	ε
inverse temperature ($1/kT$)	β	ε^{-1}
(reduced) chemical potential	$\beta\mu$	-
(reduced) free energy per unit volume	$\beta\omega$	σ^{-3}
(number) density	ρ	σ^{-3}
vacancy concentration	c_{vac}	-
gaussian width parameter	α	σ^{-2}
number of grid points on cell side	N_{grid}	-
lattice constant	a_{latt}	σ
grid spacing	δ_x	σ
Van der Waals parameter	a	σ^3
hard sphere diameter	d, d_{hs}	σ
potential cut-off	r_c	σ
potential energy parameter	ε	ε
potential length parameter	σ	σ

Table A.1 – Symbols and units used for the most common quantities encountered in this work and often associated with numerical values.

quantity	symbol
GC distribution function	f, f_N
GC partition function	Ξ
GC free energy (quantity or density functional)	Ω
Helmholtz free energy (density functional)	F
Functional of the external field, thermal length	Λ
external field	ϕ
chemical potential	μ
pressure	p
volume	V
number of particles	N
position in space	\mathbf{r}, \mathbf{q}
momentum	\mathbf{p}
Boltzmann constant	k
Planck constant (reduced)	\hbar (\hbar)
FMT local excess free energy function	Φ
FMT density averages (volume, surface, vectorial)	η, s, \mathbf{v}
pair potential	v
pair potential (repulsive part)	v_0
pair potential (attractive part)	w

Table A.2 – Symbols used for the most common quantities encountered in this work, outside of numerical context.

abbreviation	meaning
CNT	Classical Nucleation Theory
MeNT	Mesoscopic Nucleation Theory
DFT	Density Functional Theory
GC	Grand Canonical (statistical ensemble)
FMT	Fundamental Measure Theory
(m)RSLT	(modified) Bounded functional from Rosenfeld et al.
WBI(WBII)	White Bear I (II) (function or functional)
BH	Barker-Henderson (potential split convention)
WCA	Weeks-Chandler-Anderson (potential split convention)
LJ	Lennard-Jones (potential)
WHDF	Wang-Hinestrosa-Dobnikar-Frenkel (potential)
FCC	Face-Centred Cubic (Bravais lattice)
HCP	Hexagonal Closed-Packed (Bravais lattice)
DCF	Direct Correlation Function
PDF	Pair Distribution Function
GSL	GNU Scientific Library

Table A.3 – Abbreviations used in this work.

A.3 List of abbreviations

See table A.3 for a list of the most commonly used abbreviations in this work.

Appendix B

Computation details for chapter 2

B.1 Separation of the field-independent part of the free energy functional

In section 2.4, we claimed that the grand canonical free energy density functional can be separated into a simple part containing the dependence on the external field and a new functional that only depends on the density. To show this, we start from the original expression of the DFT functional (2.6), expressed using the density field,

$$\Omega[\rho; \phi_0] = \Omega[\phi_0] + k_B T \sum_{N=0}^{\infty} \int d\mathbf{q}^N \int d\mathbf{p}^N f_N[\phi[\rho]] \ln \frac{f_N[\phi[\rho]]}{f_N[\phi_0]}. \quad (\text{B.1})$$

We then express the grand canonical free energy using the partition function, move it under the integrals and substitute the partition function by its expression (2.3),

$$\begin{aligned} \Omega[\rho; \phi_0] &= k_B T \sum_{N=0}^{\infty} \int d\mathbf{q}^N \int d\mathbf{p}^N f_N[\phi[\rho]] (\ln f_N[\phi[\rho]] - \ln f_N[\phi_0] - \ln \Xi[\phi_0]), \\ &= k_B T \sum_{N=0}^{\infty} \int d\mathbf{q}^N \int d\mathbf{p}^N f_N[\phi[\rho]] \cdots \\ &\quad \cdots \left(\ln f_N[\phi[\rho]] + \ln(N! h^{DN}) + \beta \hat{K}_N + \beta \hat{V}_N + \beta \hat{U}_N - \beta \mu N \right), \\ &= \sum_{N=0}^{\infty} \int d\mathbf{q}^N \int d\mathbf{p}^N f_N[\phi[\rho]] \left(\hat{K}_N + \hat{V}_N + k_B T \ln(N! h^{DN}) + k_B T \ln f_N[\phi[\rho]] \right) \\ &\quad + \int d\mathbf{r} (\phi_0(\mathbf{r}) - \mu) \rho(\mathbf{r}). \end{aligned} \quad (\text{B.2})$$

The first term is a new functional $F[\rho]$ independent of the reference field ϕ_0 and the second contains the dependence on ϕ_0 ,

$$\Omega[\rho; \phi_0] = F[\rho] + \int d\mathbf{r} (\phi_0(\mathbf{r}) - \mu)\rho(\mathbf{r}), \quad (\text{B.3})$$

with

$$F[\rho] = \sum_{N=0}^{\infty} \int d\mathbf{q}^N \int d\mathbf{p}^N f_N[\phi[\rho]] \left(\hat{K}_N + \hat{V}_N + k_B T \ln(N! h^{DN}) + k_B T \ln f_N[\phi[\rho]] \right). \quad (\text{B.4})$$

B.2 Integration of the Euler-Lagrange equation: The density functional of the ideal gas

For exactly solvable systems, the Euler-Lagrange equation (2.14) can be integrated to give an exact expression of the free energy functional. In this section, we derive the functional for the ideal gas, which appears in the DFT model (3.2).

The integration of the Euler-Lagrange equation is possible because we can find an exact relation between the local density and the external field. This relation is obtained by deriving the grand potential, for which we have an exact expression. Keeping the general notations of section 2.2, we show that the functional derivative of the grand potential with respect to the external field is

$$\begin{aligned} \frac{\delta \Omega[\rho]}{\delta \phi(\mathbf{r})} &= -\frac{kT}{\Xi[\rho]} \frac{\delta \Xi[\rho]}{\delta \phi(\mathbf{r})}, \\ &= -\frac{kT}{\Xi[\rho]} \frac{\delta}{\delta \phi(\mathbf{r})} \left\{ \sum_{N=0}^{\infty} \int d\mathbf{q}^N \int d\mathbf{p}^N \frac{1}{N! h^{DN}} e^{-\beta(\hat{H}_N - \mu N)} \right\}, \\ &= -\frac{kT}{\Xi[\rho]} \sum_{N=0}^{\infty} \int d\mathbf{q}^N \int d\mathbf{p}^N \frac{1}{N! h^{DN}} e^{-\beta(\hat{H}_N - \mu N)} (-\beta) \frac{\delta \hat{H}_N}{\delta \phi(\mathbf{r})}, \\ &= \frac{1}{\Xi[\rho]} \sum_{N=0}^{\infty} \int d\mathbf{q}^N \int d\mathbf{p}^N \frac{1}{N! h^{DN}} e^{-\beta(\hat{H}_N - \mu N)} \frac{\delta \hat{U}_N}{\delta \phi(\mathbf{r})}. \end{aligned} \quad (\text{B.5})$$

We can use the functional expression of \hat{U}_N (2.2) to show that its functional deriva-

tive with respect to ϕ is the density operator $\hat{\rho}$. The substitution gives

$$\begin{aligned}\frac{\delta\Omega[\rho]}{\delta\phi(\mathbf{r})} &= \frac{1}{\Xi[\rho]} \sum_{N=0}^{\infty} \int d\mathbf{q}^N \int d\mathbf{p}^N \frac{1}{N!h^{DN}} e^{-\beta(\hat{H}_N - \mu N)} \hat{\rho}(\mathbf{r}), \\ &= \sum_{N=0}^{\infty} \int d\mathbf{q}^N \int d\mathbf{p}^N f(\mathbf{q}^N, \mathbf{p}^N, N, [\phi]) \hat{\rho}(\mathbf{r}), \\ &= \langle \hat{\rho}(\mathbf{r}) \rangle \equiv \rho(\mathbf{r}; [\phi]).\end{aligned}\tag{B.6}$$

For the ideal gas, the partition function is

$$\begin{aligned}\Xi[\rho] &= \sum_{N=0}^{\infty} \int d\mathbf{q}^N \int d\mathbf{p}^N \frac{1}{N!h^{DN}} \exp \left\{ -\beta \sum_{i=1}^N \left(\frac{\mathbf{p}_i^2}{2m} + \phi(\mathbf{q}_i) \right) + \beta\mu N \right\}, \\ &= \sum_{N=0}^{\infty} \frac{1}{N!} \left(\frac{1}{h^D} \int d\mathbf{q} \int d\mathbf{p} \exp \left\{ -\beta \frac{\mathbf{p}^2}{2m} - \beta\phi(\mathbf{q}) + \beta\mu \right\} \right)^N, \\ &= \sum_{N=0}^{\infty} \frac{1}{N!} \left(\Lambda^{-D} \int d\mathbf{q} \exp \{ -\beta(\phi(\mathbf{q}) - \mu) \} \right)^N \quad \text{with} \quad \Lambda = \frac{h}{\sqrt{2\pi mkT}}, \\ &= \exp \left(\Lambda^{-D} \int d\mathbf{q} \exp \{ -\beta(\phi(\mathbf{q}) - \mu) \} \right).\end{aligned}\tag{B.7}$$

The grand canonical free energy is therefore

$$\Omega[\phi] = -kT \Lambda^{-D} \int d\mathbf{q} \exp \{ -\beta(\phi(\mathbf{q}) - \mu) \} \tag{B.8}$$

and the density

$$\rho(\mathbf{r}; [\phi]) = \frac{\delta\Omega[\rho]}{\delta\phi(\mathbf{r})} = \Lambda^{-D} \exp \{ -\beta(\phi(\mathbf{q}) - \mu) \}. \tag{B.9}$$

From this, we isolate $\phi(\mathbf{q}) - \mu$ and replace it in the Euler-Lagrange equation:

$$\frac{\delta\beta F_{id}[\rho]}{\delta\rho(\mathbf{r})} = \mu - \phi(\mathbf{r}) = kT \ln \{ \rho(\mathbf{r}) \Lambda^D \}. \tag{B.10}$$

The Euler-Lagrange equation is then integrated on a linear path from 0 to $\rho(\mathbf{r})$:

$$\begin{aligned}F_{id}[\rho] &= \int_0^1 d\lambda \int d\mathbf{r} \lambda \rho(\mathbf{r}) \frac{\delta\beta F_{id}[\rho]}{\delta\lambda\rho(\mathbf{r})} = \int_0^1 d\lambda \int d\mathbf{r} \rho(\mathbf{r}) \ln \{ \lambda \rho(\mathbf{r}) \Lambda^D \} \\ &= \int d\mathbf{r} (\rho(\mathbf{r}) \ln \{ \rho(\mathbf{r}) \Lambda^D \} - \rho(\mathbf{r})).\end{aligned}\tag{B.11}$$

B.3 The uniform density limit of the mRSLT functional and the Carnahan-Starling equation of state

In section 3.3, we computed the uniform limit of the mRSLT functional (3.12). We got

$$\Phi(\eta, s, \mathbf{v}) = \rho \frac{\eta(4 - 3\eta)}{(1 - \eta)^2}. \quad (\text{B.12})$$

The expression of the free energy per unit volume for a hard sphere fluid is thus (see equation 3.14 with $a = 0$)

$$\beta\omega(\rho) = \rho \ln \rho - \rho + \rho \frac{\eta(4 - 3\eta)}{(1 - \eta)^2} - \beta\mu\rho \quad (\text{B.13})$$

and its derivative is

$$\beta \frac{\partial \omega(\rho)}{\partial \rho} = \ln \rho + \frac{\eta(3\eta^2 - 9\eta + 8)}{(1 - \eta)^3} - \beta\mu. \quad (\text{B.14})$$

At the equilibrium density $\partial\omega/\partial\rho = 0$ and we can isolate the chemical potential,

$$\beta\mu = \ln \rho + \frac{\eta(3\eta^2 - 9\eta + 8)}{(1 - \eta)^3}, \quad (\text{B.15})$$

and substitute this expression in (B.13) to get

$$\begin{aligned} \beta\omega/\rho &= -1 + \rho \frac{\eta(4 - 3\eta)}{(1 - \eta)^2} - \frac{\eta(3\eta^2 - 9\eta + 8)}{(1 - \eta)^3}, \\ &= -\frac{1 - 3\eta + 3\eta^2 - \eta^3 - 4\eta + 3\eta^2 + 4\eta^2 - 3\eta^3 + 3\eta^3 - 9\eta^2 + 8\eta}{(1 - \eta)^3}, \\ &= -\frac{1 + \eta + \eta^2 - \eta^3}{(1 - \eta)^3}. \end{aligned} \quad (\text{B.16})$$

We then write this in terms of the pressure, which is minus the free energy per unit volume. We get the Carnahan-Starling equation of state [23] for the pressure in a hard sphere fluid,

$$\beta p/\rho = \frac{1 + \eta + \eta^2 - \eta^3}{(1 - \eta)^3}. \quad (\text{B.17})$$

Appendix C

Free energy landscape for gaussian profiles

In this appendix, we present a few more graphs of the free energy landscape presented in section 3.6. These free energy landscapes shows the values of the free energy functional across a broad range of the vacancy concentration, c_{vac} , and the gaussian width parameter α . In particular, they show the location of the solid minimum and its position relative to the singular region, where our implementation of the functional diverges ¹.

Figure C.1 reports free energy landscapes for the Lennard-Jones potential at a few different temperatures. We see that the region where the functional diverges depend neither on the temperature nor on the number of grid points N_{grid} , at least not significantly. It is located at low vacancy concentrations and high values of the gaussian width parameter α , which corresponds to narrow peaks in the density. These figures indicate that the singular region overlaps the valley of the solid minimum only at low temperatures. We therefore expect no valid results for the vacancy concentration at low temperatures. This is confirmed in the data we presented in the chapter on vacancy concentrations (see Fig. 7.1). The same behaviour applies to the WHDF $r_c = 2$ potential, as shown on Fig. C.2.

The last graph in Fig. C.1 tell us that we can get rid of the singular region using the analytical evaluation of the spherical integrals developed by Lutsko (cf. section 3.2). However, the situation is more complex for the WHDF $r_c = 1.2$ potential modelling colloids. In this case, Fig. C.3 shows two regions where the free energy functional diverges. The first is the same that we observe for the other potentials, due to the way we perform spherical integrations. The second is located at high values of the gaussian width parameter α and affects all vacancy concentrations. It starts around $\alpha = 10^3$, a region that was not explored for the other potentials. This corresponds to very narrow peaks in the density profile. Therefore, the divergence

¹cf. discussion in section 3.6 on the origin of the singularities.

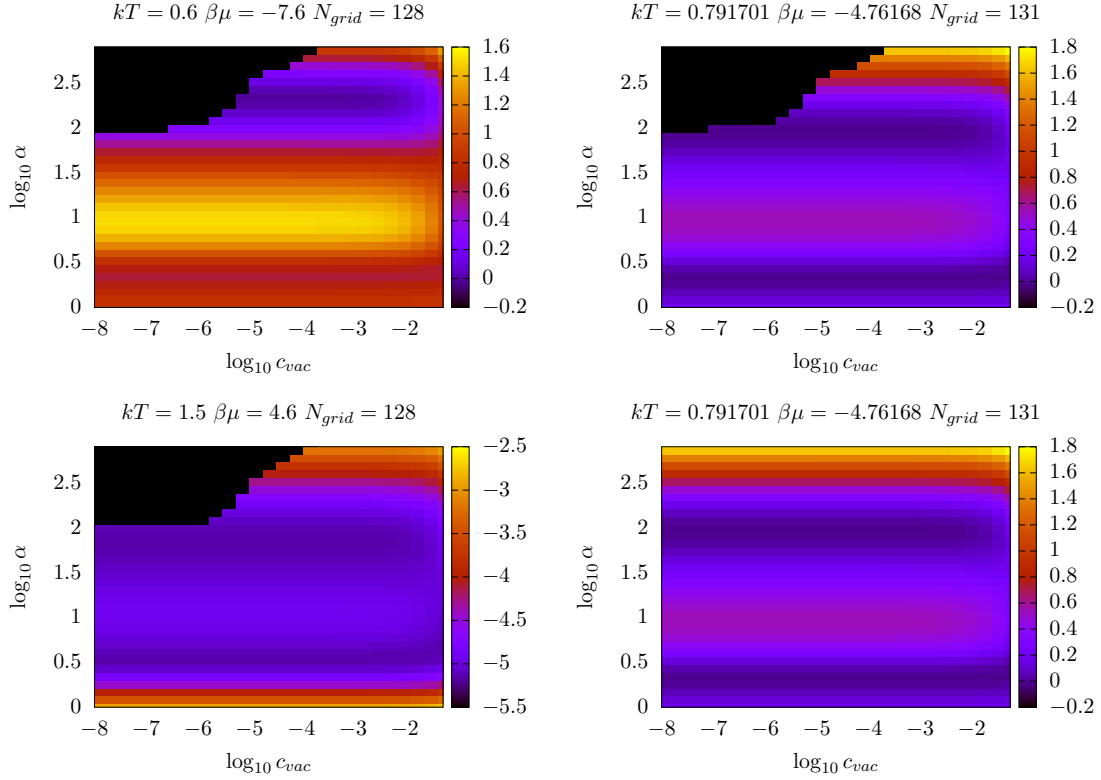


Figure C.1 – Typical landscape of free energy functional for the LJ potential, using a cut-off $r_c = 3$. All of these graphs have been computed using numeric weights for the spherical integration, except the bottom right one for which we used the analytic evaluation of the spherical integrals developed by Lutsko (cf. section 3.2). The black colour represents unsuccessful computations, outlining the region where the functional diverges.

is likely caused by the loss of accuracy² as too few grid points are located on the density peak. A quick calculation can tell us the order of magnitude for α above which the grid spacing becomes inadequate. The grid spacing δ_x is too large when it is about the same size as the width σ of the gaussian profile. Using the value we used for the grid spacing, $\delta_x = 0.0125$, we recover the observed limit

$$\alpha = \frac{1}{2\sigma^2} \approx \frac{1}{2\delta_x^2} = \frac{80^2}{2} = 3200 \approx 10^3. \quad (\text{C.1})$$

The second divergence region (high values of α) could be eliminated by working with a finer grid, but at the cost of significant increase of the computation time. In our case, we identified the problem too late to restart with a finer grid. The impact of this limitation is not visible on phase diagrams. It only affects more sensitive calculations, like the computation of vacancies or the free energy difference between the FCC and HCP configurations, which are discussed in chapter 7 and 8.

²To understand how low accuracy can lead to failures in calculations, see again the discussion in section 3.6 for the origin of the singularities.

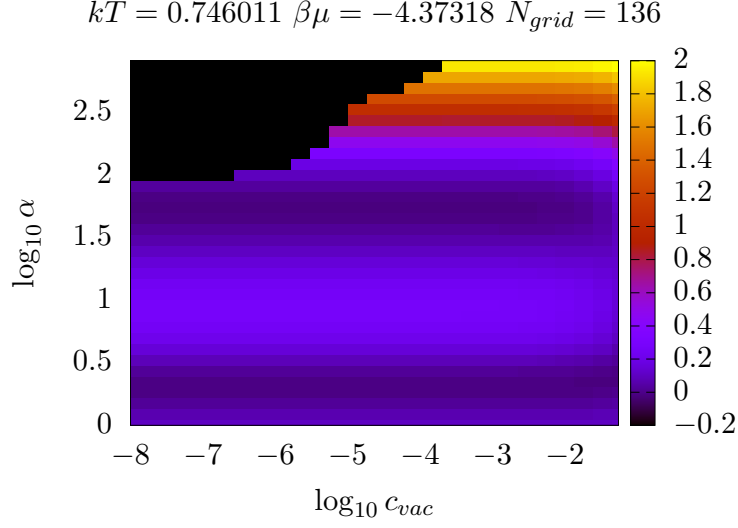


Figure C.2 – Typical landscape of free energy functional for the WHDF potential, using a cut-off $r_c = 2$. This graph has been computed using numeric weights for the spherical integration. The black colour represents unsuccessful computations, outlining the region where the functional diverges.

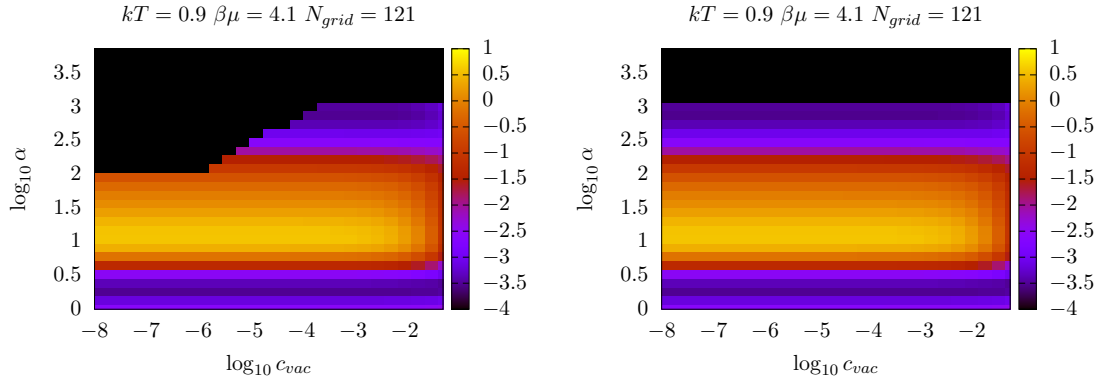


Figure C.3 – Typical landscape of free energy functional for the WHDF potential, using a cut-off $r_c = 1.2$. The graph on the left has been computed using numeric weights for the spherical integration and the graph on the right using the analytical evaluation developed by Lutsko (see section 3.2). The black colour represents unsuccessful computations, outlining the region where the functional diverges.

Appendix D

Code repository

For transparency and so that anyone can reproduce the results presented in this work, the source code is available on GitHub at the following address:

`https://github.com/ceschoon/Memoire`.

This repository contains the code necessary to generate all the data presented in this master's thesis. In particular, the numerical values behind the figures of this document can be found in the form of plain text files.

Bibliography

- [1] P. T. Lansbury Jr. J. D. Harper C. M. Lieber. “Atomic force microscopic imaging of seeded fibril formation and fibril branching by the Alzheimer’s disease amyloid-b protein”. *Chem. Biol.* 4 (), pp. 951–959 (cit. on p. 6).
- [2] G. B. Benedek M. M. Condrón D. B. Teplow D. M. Walsh A. Lomakin. “Amyloid b-protein fibrillogenesis. Detection of a protofibrillar intermediate”. *Chem. Biol.* 272 (), 22364–22372 (cit. on p. 6).
- [3] J. D. Rimer P. G. Vekilov K. N. Olafson T. Q. Nguyen. “Antimalarials inhibit hematin crystallization by unique drug–surface site interactions”. *Proc. Natl. Acad. Sci. U.S.A.* 114 (), pp. 7531–7536 (cit. on p. 6).
- [4] A. S. Myerson D. Erdemir A. Y. Lee. “Polymorph selection: The role of nucleation, crystal growth and molecular modeling”. *Curr. Opin. Drug Discov. Dev.* 10 (), 746–755 (cit. on p. 7).
- [5] H. Cölfen D. Gebauer A. Volkel. “Stable prenucleation calcium carbonate clusters”. *Science* 322 (2008), pp. 1819–1822 (cit. on pp. 7, 10).
- [6] G. Nicolis J. F. Lutsko. “Theoretical Evidence for a Dense Fluid Precursor to Crystallization”. *Phys. Rev. Lett.* 96.046102 (2006). URL: http://jimlutsko.github.io/files/Lutsko_PRL_2006_1.pdf (cit. on pp. 7, 10, 44).
- [7] A. D. Dinsmore J. R. Savage. “Experimental evidence for two-step nucleation in colloidal crystallization”. *Phys. Rev. Lett.* 102.198302 (2009) (cit. on pp. 7, 10).
- [8] A. E. S. Van Driessche M. Sleutel. “Role of clusters in nonclassical nucleation and growth of protein crystals”. *Proc. Natl. Acad. Sci. U.S.A.* 111 (2014), E546–E553 (cit. on pp. 7, 10).
- [9] D. Kashchiev. *Nucleation: Basic Theory with Applications*. 1st ed. Butterworth-Heinemann, 2000 (cit. on p. 8).
- [10] *New perspectives on Mineral Nucleation and Growth*. 1st ed. Springer, 2017. URL: <https://doi.org/10.1007/978-3-319-45669-0> (cit. on p. 8).
- [11] J. F. Lutsko. “How crystals form: A theory of nucleation pathways”. *Science Advances* 5.eaav7399 (2019). URL: <http://advances.sciencemag.org/content/5/4/eaav7399> (cit. on pp. 9, 10, 64).

- [12] J. F. Lutsko. “A dynamical theory of nucleation for colloids and macromolecules”. *J. Chem. Phys.* 136.034509 (2012). URL: http://jimlutsko.github.io/files/Lutsko_JCP_2012_1.pdf (cit. on pp. 9, 10).
- [13] J. Lam J. F. Lutsko. “Classical density functional theory, unconstrained crystallization, and polymorphic behavior”. *Phys. Rev. E* 98 (2018). URL: http://jimlutsko.github.io/files/Lutsko_PRE_2018.pdf (cit. on pp. 9, 10, 19, 20, 64).
- [14] D. Frenkel P. R. ten Wolde. “Enhancement of protein crystal nucleation by critical density fluctuations”. *Science* 77 (1997), 1975–1978 (cit. on p. 10).
- [15] P. G. Vekilov O. Galkin. “Control of protein crystal nucleation around the metastable liquid–liquid phase boundary”. *Proc. Natl. Acad. Sci. U.S.A.* 97 (2000), 6277–6281 (cit. on p. 10).
- [16] James F. Lutsko. *classicalDFT library*. commit 9b5e7e6e5f0140b4cbc87a15-de89753ad89e5144. URL: <https://github.com/jimlutsko/classicalDFT> (cit. on pp. 10, 24).
- [17] J. Dobnikar D. Frenkel X. Wang S. Ramírez-Hinestrosa. “The Lennard-Jones potential: when (not) to use it”. *Phys. Chem. Chem. Phys.* (2020). URL: <http://dx.doi.org/10.1039/C9CP05445F> (cit. on pp. 11, 29, 39, 43, 45, 57, 60).
- [18] W. Kohn P. Hohenberg. “Inhomogeneous Electron Gas”. *Phys. Rev.* 136 (3B 1964), B864–B871. URL: <https://link.aps.org/doi/10.1103/PhysRev.136.B864> (cit. on p. 14).
- [19] D. N. Mermin. “Thermal Properties of the Inhomogeneous Electron Gas”. *Phys. Rev.* 137 (5A 1965), A1441–A1443. URL: <https://link.aps.org/doi/10.1103/PhysRev.137.A1441> (cit. on p. 15).
- [20] Y. Rosenfeld. “Free-energy model for the inhomogeneous hard-sphere fluid mixture and density-functional theory of freezing”. *Phys. Rev. Lett.* 63 (9 1989), pp. 980–983. URL: <https://link.aps.org/doi/10.1103/PhysRevLett.63.980> (cit. on p. 18).
- [21] P. Tarazona. “Density Functional for Hard Sphere Crystals: A Fundamental Measure Approach”. *Phys. Rev. Lett.* 84 (4 2000), pp. 694–697. URL: <https://link.aps.org/doi/10.1103/PhysRevLett.84.694> (cit. on p. 19).
- [22] A. Lang G. Kahl R. Roth R. Evans. “Fundamental measure theory for hard-sphere mixtures revisited: the White Bear version”. *Journal of Physics: Condensed Matter* 14.46 (2002), pp. 12063–12078. URL: <https://doi.org/10.1088%2F0953-8984%2F14%2F46%2F313> (cit. on p. 19).
- [23] K.E. Starling T.W. Leland G.A. Mansoori N.F. Carnahan. “Equilibrium Thermodynamic Properties of the Mixture of Hard Spheres”. *The Journal of Chemical Physics* 54.4 (1971), pp. 1523–1525. URL: <https://doi.org/10.1063/1.1675048> (cit. on pp. 19, 71).

- [24] H. Lowen Y. Rosenfeld M. Schmidt and P. Tarazona. “Fundamental-measure free-energy density functional for hard spheres: Dimensional crossover and freezing”. *Phys. Rev. E* 55 (4 1997), pp. 4245–4263. URL: <https://link.aps.org/doi/10.1103/PhysRevE.55.4245> (cit. on p. 20).
- [25] D. Henderson J.A. Barker. “Perturbation Theory and Equation of State for Fluids. II. A Successful Theory of Liquids”. *The Journal of Chemical Physics* 47.11 (1967), pp. 4714–4721. URL: <https://doi.org/10.1063/1.1701689> (cit. on p. 21).
- [26] H.C. Andersen J.D. Weeks D. Chandler. “Role of Repulsive Forces in Determining the Equilibrium Structure of Simple Liquids”. *The Journal of Chemical Physics* 54.12 (1971), pp. 5237–5247. URL: <https://doi.org/10.1063/1.1674820> (cit. on p. 21).
- [27] J. F. Lutsko. “Recent Developments in Classical Density Functional Theory”. *Adv. Chem. Phys.* 144 (2010). URL: http://jimlutsko.github.io/files/Lutsko_DFT_Review.pdf (cit. on p. 21).
- [28] I. McDonald J.-P. Hansen. *Theory of Simple Liquids*. 3rd ed. Acad. Press, San Diego, CA, 2006, pp. 116–118 (cit. on p. 21).
- [29] *GNU Scientific Library, version 2.4*. URL: <https://www.gnu.org/software/gsl/> (cit. on pp. 26, 32, 37, 38).
- [30] D.A.Kofke A.J. Schultz. “Comprehensive high-precision high-accuracy equation of state and coexistence properties for classical Lennard-Jones crystals and low-temperature fluid phases”. *The Journal of Chemical Physics* 149.20 (2018), p. 204508. URL: <https://doi.org/10.1063/1.5053714> (cit. on pp. 29, 40, 43).
- [31] *Web Plot Digitizer 4.2*. URL: <https://apps.automeris.io/wpd/> (cit. on pp. 40, 54, 56).
- [32] F. Rosenberger M. Muschol. “Liquid–liquid phase separation in supersaturated lysozyme solutions and associated precipitate formation/crystallization”. *The Journal of Chem. Phys.* 107.1953 (1997). URL: <http://dx.doi.org/10.1063/1.474547> (cit. on p. 45).
- [33] S.G. Moustafa J.R. Errington D.A. Kofke A. Purohit A.J. Schultz. “Free energy and concentration of crystalline vacancies by molecular simulation”. *Molecular Physics* 116.21-22 (2018), pp. 3027–3041. URL: <https://doi.org/10.1080/00268976.2018.1481542> (cit. on pp. 54, 56).
- [34] A.D.J. Haymet R. McRae J.D. McCoy. “Density functional theory of vacancies”. *The Journal of Chemical Physics* 93.4281 (1990). URL: <https://doi.org/10.1063/1.458708> (cit. on pp. 55, 56).
- [35] S. P. Das S. P. Singh. “Density functional theory of vacancies”. *Phys. Rev. B* 75.144113 (2007). URL: <https://doi.org/10.1103/PhysRevB.75.144113> (cit. on pp. 55, 56).

